RESEARCH ARTICLE

VOLCANICA

Post-glacial melt generation in Southern Chile and the development of the Carrán-Los Venados Volcanic Field (40°20'S)

Lucy McGee *[α], Katy J. Chamberlain[β], Mark Reagan[γ], Geoff Nowell[δ], and Luis E. Lara[ε,ζ]

[α] Department of Earth Sciences, Adelaide University, Adelaide, South Australia.
[β] Department of Earth, Ocean & Ecological Sciences, University of Liverpool, Liverpool, UK.
[γ] Department of Earth & Environmental Sciences, The University of Iowa, Iowa City, USA.
[δ] Department of Earth Sciences, Durham University, Durham, UK.
[ε] Instituto de Ciencias de la Tierra, Facultad de Ciencias, Universidad Austral de Chile, Valdivia, Chile.
[ζ] Millenium Nucleus Ckelar Volcanes, Chile.

Submitted: 2025-02-01 | Accepted: 2025-11-13 | Published: 2026-02-11

Editor: J. Browning | Typesetter: A. Ryan

Abstract

The Carrán-Los Venados volcanic field in southern Chile comprises small basaltic eruption centres of Holocene to historical ages. These centres are atop extensive, basaltic flows that erupted during late glacial or early postglacial times (< 14ka), marking a dramatic change in eruption style over a short space of time. Differences in trace element characteristics and U-series isotopes point to a dampened subduction influence in the melting environment of the older Basal Lavas. Th isotopes point to higher melting rates and more dominant decompression melting, which may be related to the deglaciation of southern Chile at this time. Olivine textures and chemistry suggest longer storage times for the Basal Lavas compared to the Holocene tephras. The historic eruptions have relatively homogeneous whole rock compositions, suggesting the development of a storage system in the lower crust. This may be the beginning of a thermal environment more akin to those of nearby stratovolcanoes.

Keywords: Basalt; Monogenetic; U-series; Olivine; Sr-Nd-Pb Isotopes; Deglaciation.

1 Introduction

Studies of arc volcanism often focus on large-volume andesitic stratovolcanoes, yet wide ranges in the styles and volumes of volcanic edifices are found in arcs such as the Chilean Southern Volcanic Zone (SVZ) [e.g. Cembrano and Lara 2009]. This range of eruption styles and edifice building reflects differences in the compositions of parental magmas, the rates at which these magmas are generated, and their chemical and physical interactions with crust on their way to the surface ultimately affecting the hazard from eruptions [e.g. Edmonds et al. 2019]. Unravelling processes associated with magma generation in the mantle from those occurring in the crust is challenging [e.g. Hildreth and Moorbath 1988; Stern et al. 1991; Mamani et al. 2009; Turner et al. 2017] and the crustal involvement may change over time as volcanic systems develop and grow [e.g. Singer et al. 2008]. Understanding this evolution is vital to better forecast future eruptive activity in active arc systems [e.g. Albert et al. 2016], especially if a magmatic system appears to be growing more extensive or exhibit more frequent eruptive behaviour. Analysis of dispersed, small-volume monogenetic volcanism [Németh and Kereszturi 2015; Cañón-Tapia 2016; McGee and Smith 2016] where a time sequence of eruptions can be deduced offers an opportunity to investigate how magma genesis and differentiation processes evolve as volcanic regions develop.

To unravel these processes, detailed whole rock [e.g. Rasoazanamparany et al. 2016; Ancellin et al. 2017; McGee et al. 2017; Larrea et al. 2019] and mineral-specific compositional data are needed [e.g. Jankovics et al. 2019; Winslow et al. 2020; Ruth and Costa 2021]. Combined long-lived isotope data and decamillennial to centamillennial sensitive ^{238}U-^{234}U-^{230}Th data are particularly valuable for understanding the evolution of sources and time-frame of crustal processing in arc environments [e.g. Reagan et al. 2003; Jicha et al. 2007]. In arc environments, high (^{238}U/^{232}Th) values (where parentheses denote activity ratios) can chart slab fluid involvement in generating arc magmas [Turner et al. 2003], and the extent of preserved U-series disequilibria and Th isotope data can be used to determine the competing processes (and their associated timescales) related to crustal processing [Condomines et al. 2003; Turner et al. 2003; McGee et al. 2019; Godoy et al. 2020].

Arc-wide studies of the origins of lavas that build stratovolcanoes have been undertaken in the Southern Volcanic Zone (SVZ) of Chile, and evidence for both along-strike and temporal variations in lava compositions is seen [Watt et al. 2013; Jacques et al. 2014; Hickey-Vargas et al. 2016a; Hickey-Vargas et al. 2016b; Turner et al. 2016; McGee et al. 2017]. Yet, how variations in mantle compositions, melting dynamics, and crustal processing impacts the surface expressions of SVZ magmatism (and associated hazards) remain relatively poorly understood. In several locations in the SVZ more extensive Basal Lavas are observed as the first eruptive product before development of small eruptive centres (SECs), for example in the Caburgua-Huelemolle small eruptive centres near the Villarrica stratovolcano [Cembrano and Lara 2009]. Such 'Basal Lavas' also lie beneath the Carrán-Los Venados (CLV) volcanic field in the SVZ and provide an opportunity to assess the temporal evolution of mantle melting dynamics over the last c. 14 kyr, where surface expression of magmatism changed from the eruption of relatively large volume Basal Lavas to the dispersed volcanism of the CLV volcanic field, which has approximately 65 SECs [Bucchi et al. 2015].

* lucy.mcgee@adelaide.edu.au

To constrain the relationship between the older interglacial Basal Lavas and the Holocene postglacial Carrán-Los Venados SECs, we present detailed whole rock geochemical data, including major and trace element concentrations coupled with Sr-Nd-Pb and U-Th isotopic measurements. These whole rock data are supplemented with textural observations of thin sections and *in situ* major element analyses of macrocrystic mineral phases. By combining geochemical data with models of mantle melting and the temporal relationships of sampled eruptive centres we elucidate the changing mantle composition and melting processes between eruption of the Basal Lavas and the dispersed monogenetic field of CLV. We also compare recent (1907–1979 CE) eruptions from Carrán-Los Venados to test for systematic changes over human timescales and speculate on the potential future development of the CLV system.

2 Background and Setting

The subduction of the Nazca plate beneath the South American plate and the arc-parallel Liquiñe-Ofqui fault system (Figure 1) both exert control on the location of stratovolcanoes and smaller, monogenetic systems in the southern Andes [Lara et al. 2006; Cembrano and Lara 2009]. Southern Chile contains numerous fields of small eruptive centres in addition to its prominent stratovolcanoes. These two volcanic styles frequently co-exist, such as in the Pucón area, which is close to the active stratovolcano Villarrica [Morgado et al. 2015; Hickey-Vargas et al. 2016a; McGee et al. 2017], the Fui group small eruptive centres next to the stratovolcano Mocho-Choshuenco [Mallea-Lillo et al. 2022; 2025], the Puerto Varas area, which has the recently active Calbuco volcano nearby [López-Escobar et al. 1995; Morgado et al. 2022], the Hudson volcano and associated monogenetic centres in Patagonia [Gutiérrez et al. 2005], and the CLV volcanic field, which is located at 40°21' S in the Central Southern Volcanic Zone of the Andes, 30 km north of the Puyehue-Cordón Caulle stratovolcano complex (PCC; Figure 1).

The general features of the volcanic field have been well-described by Bucchi et al. [2015], who compared the stress field and related structures of the CLV volcanic field to the PCC stratovolcano. Basement rocks in the area are dominantly intrusive rocks of Paleocene to Miocene age. Filling the valleys and underlying the volcanic field are the relatively voluminous 'Basal Lavas', whose original vents are likely buried by the CLV volcanic field [Bucchi et al. 2015]. These lavas do not show evidence of glacial erosion therefore are interpreted to be < 13.9 ka in age [e.g. Campos et al. 1998; Bucchi et al. 2015; Rawson et al. 2016]. The main CLV field comprises approximately 65 eruptive vents as basaltic scoria cones and associated lava flows or maars (Figure 1C and Figure 2). Bucchi et al. [2015] obtained radiocarbon dates on material in successions of pyroclastic falls and paleosols with dates ranging from 225 ± 75 to 3720 ± 30 yrs BP. There have been three historic eruptions in the CLV field (Figure 1C): Riñinahue (1907 CE, a maar infilled with lava flows), Carrán (1955 CE, a maar) and Mirador (1979 CE, a scoria cone and lava flow, described in López-Escobar and Moreno [1981]). Volcanism in the field therefore dates from early post-glacial to historic and covers a range of eruptive styles.

3 Methods and Materials

3.1 Sampling

An overview of the samples is given in Table 1. Three samples of Basal Lava flows beneath the CLV field were taken from river exposures (one location shown in Figure 2A), and one sample (FB091012-7) previously collected and reported in Bucchi et al. [2015] was added to this (location given in Table 1). Sixteen tephras representing Holocene scoria cone-building eruptions referred to here as 'Holocene tephras' were taken from four separate road cuts (two of these are shown in Figure 2B and Figure 2C, locations given in Table 1). Five scoria, 2 bombs and 8 samples of lava from the Mirador eruption were sampled through the eruptive sequence (Figure 2D–E). Three lapilli samples were also taken from the lake edge of Pocura maar (Figure 2F). The sample from Riñinahue (VTL-29) was collected from *in situ* exposure of the edifice, see details in Chamberlain et al. [2024]. Pocura, Riñinahue and Mirador are collectively referred to as the 'historic eruptions'.

3.2 Whole rock major and trace elements

The samples were first washed in distilled water and dried in sample ovens at 100 °C for a day, then crushed and milled in tungsten carbide at the Universidad de Chile. All samples were analysed for major and trace elements at the commercial laboratory Actlabs Inc. (Canada). Major elements and the trace elements Sc, V, Ba, Sr, Y, Zr were analysed by fusion inductively coupled plasma (ICP) analysis. Samples were mixed with a flux of lithium metaborate and lithium tetraborate and fused in a furnace; the liquid sample was then mixed into a 5 % HNO_3 solution containing an internal standard and analysed on a Thermo Jarrell-Ash ENVIRO II ICP mass spectrometer (MS). These solutions were then diluted and analysed for trace element content (Cr, Co, Ni, Cu, Zn, Ga, Rb, Nb, Cs, La, Ce, Pr, Nd, Sm, Eu, Gd, Tb, Dy, Ho, Er, Tm, Yb, Lu, Hf, Ta, Pb, Th, U) on a Perkin Elmer Sciex ELAN ICP MS. In addition to the suite of standard material which Actlabs includes in the analyses (which include USGS standard BIR-1a), USGS standards BCR-2 and BHVO-2 were included as unknowns in the sample set and are in general < 5 % offset from the GeoRem preferred values, with the exception of Cr, Y and U in BCR-2, and Ga, Nb and Hf in both standards. A method blank was below detection limit in all elements and two samples were duplicated with excellent precision (generally < 5 %, and all < 10 % with the exception of Y in both (10.5–24 % offset) and Zn in one (12.5 % offset)). Two samples from the dataset (a Basal Lava BL16-2 and lava from Mirador VM15-8) were analysed at Washington State University (WSU) as a comparison to the Actlabs data. The Mirador lava compares excellently; transition metal analyses in the Basal Lava are measured as somewhat higher by WSU, and larger discrepancies are seen for elements in low abundance. All data are presented in Supplementary Material 1 including USGS standards analysed at Actlabs, WSU comparison and duplicates.

Table 1: Samples analysed in this study. Full whole rock major, trace and isotopic element analyses are available in Supplementary Material 1.

Volcanic Centre	Sample ID	Eruption Age (if known)	Sample Type	Location in degrees, minutes, seconds (WGS84)	SiO_2 (wt.%)	MgO (wt.%)	CaO (wt.%)	Na_2O + K_2O (wt.%)
Basal lava	BL16- 1	<13.9 ka[a]	Lava	40°17'05.0" S, 72°10'19.95" W	52.02	4.22	8.32	4.52
Basal lava	BL16- 2	<13.9 ka[a]	Lava	40°18'12.08" S, 72°09'52.46" W	51.51	4.19	8.07	4.6
Basal lava	BL16- 3	<13.9 ka[a]	Lava	40°19'32.95" S, 72°07'56.89" W	52.63	3.96	8.25	4.36
Basal lava	FB091012-7	<13.9 ka[a]	Lava	40°18'41.46" S, 72°13'26.29" W	51.13	4.42	7.89	4.45
Holocene maar (unnamed)	UM17- 1	unknown	Lapilli	40°22'08.33" S, 72°01'57.01" W	52.46	4.07	8.25	4.22
Holocene tephras	UF17- 1	unknown	Lapilli	40°22'11.82" S, 72°00'39.71" W	50.97	4.85	8.64	3.58
Holocene tephras	UF17- 2	unknown	Lapilli	40°22'10.12" S, 72°00'40.30" W	52.71	4.02	7.93	4.26
Holocene tephras	UF17- 3	unknown	Lapilli	40°22'08.86" S, 72°00'55.47" W	53.34	3.71	7.53	4.29
Holocene tephras	UF17- 4	unknown	Lapilli	40°22'08.86" S, 72°00'55.47" W	52.71	4.12	8.26	4.02
Holocene tephras	UF17- 5	unknown	Lapilli	40°22'08.39" S, 72°01'10.05" W	51.25	5.69	9.1	3.28
Holocene tephras	UF17- 6	unknown	Lapilli	40°22'04.83" S, 72°01'34.37" W	53.61	5.7	8.18	3.93
Holocene tephras	UF17- 7	unknown	Lapilli	40°22'04.83" S, 72°01'34.37" W	51.3	5.51	8.94	3.17
Holocene tephras	UF17- 8	unknown	Lapilli	40°22'04.83" S, 72°01'34.37" W	51.92	5.43	9.01	3.45
Holocene tephras	UF17- 9	unknown	Lapilli	40°22'02.20" S, 72°01'37.92" W	52.39	4.65	8.67	3.56
Holocene tephras	UF17- 10	unknown	Lapilli	40°22'02.20" S, 72°01'37.92" W	52.54	4.77	8.54	3.57
Holocene tephras	UF17- 11	unknown	Lapilli	40°22'02.20" S, 72°01'37.92" W	52.68	4.91	8.68	3.5
Holocene tephras	UF17- 11b	unknown	Lapilli	40°22'02.20" S, 72°01'37.92" W	52.32	4.97	8.53	3.82
Holocene tephras	UF17- 12	unknown	Lapilli	40°22'02.20" S, 72°01'37.92" W	53.46	4.15	8.1	4.3
Holocene tephras	UF17- 13a	unknown	Lapilli	40°22'02.20" S, 72°01'37.92" W	52.98	4.26	8.31	4.26
Holocene tephras	UF17- 14a	unknown	Lapilli	40°21'59.27" S, 72°02'01.32" W	52.48	5.07	9.13	3.8
Holocene tephras[b]	VTL-27	unknown	Tephra	40°22'11.96" S, 72°02'38.17" W	51.2	4.4	7.9	4.04
Holocene tephras[b]	VTL-28	unknown	Tephra	40°22'21.86" S, 72°03'17.79" W	51.8	4.64	7.86	4.04
Pocura maar	PM16- 1	235 yr BP ± 75 yrs[a]	Lapilli	40°21'06.60" S, 72°06'18.20" W	54.4	3.67	7.76	4.53
Pocura maar	PM16- 2	235 yr BP ± 75 yrs[a]	Lapilli	40°21'01.16" S, 72°06'11.01" W	56.14	2.85	6.83	5.1
Pocura maar	PM16- 3	235 yr BP ± 75 yrs[a]	Lapilli	40°21'01.16" S, 72°06'11.01" W	55.09	3.71	7.5	4.49
Riñinahue[b]	VTL-29	1907 CE	Lapilli	40°22'22.07" S, 72°05'06.57" W	52	4.02	7.59	4.37
Mirador	VM15- 1	1979 CE	Lava	40°21'54.68" S, 72°03'05.20" W	53.5	3.84	8	4.3
Mirador	VM15- 1B	1979 CE	Lava	40°21'52.50" S, 72°03'15.04" W	52.4	3.97	8.2	4.2
Mirador	VM15- 3	1979 CE	Lava	40°21'48.51" S, 72°03'20.30" W	52.6	4.1	8.2	4.2
Mirador	VM15- 3B	1979 CE	Lava	40°21'48.51" S, 72°03'20.30" W	52.8	4.12	8.2	4.3
Mirador	VM15- 4	1979 CE	Lava	40°21'48.79" S, 72°03'24.83" W	54.3	4.1	8.2	4.2
Mirador	VM15- 5	1979 CE	Lava	40°21'48.06" S, 72°03'26.55" W	52.7	3.88	8.1	4.3
Mirador	VM15g 6	1979 CE	Lava	40°21'48.09" S, 72°03'26.55" W	51.8	3.88	8	4.3
Mirador	VM15- 7	1979 CE	Tephra	40°21'46.80" S, 72°03'29.37" W	51.9	3.88	8	4.3
Mirador	VM15- 8	1979 CE	Lava	40°21'41.12" S, 72°03'33.06" W	51.3	3.9	8	4.4
Mirador	VM15- 9	1979 CE	Tephra	40°21'40.53" S, 72°03'32.49" W	52.9	4.22	8.3	4.3
Mirador	VM15- 10	1979 CE	Tephra	40°21'40.10" S, 72°03'35.25" W	53.1	4.22	8.3	4.4
Mirador	VM15- 11	1979 CE	Tephra	40°21'38.93" S, 72°03'32.36" W	50.9	3.93	8.1	4.4
Mirador	VM15- 12	1979 CE	Tephra	40°21'38.11" S, 72°03'32.03" W	51.7	3.83	8	4.3
Mirador	VM15- 13	1979 CE	Lava	40°21'36.81" S, 72°03'06.61" W	52.5	3.74	7.9	4.5
Mirador	VM15- B1	1979 CE	Bomb	40°21'36.61" S, 72°03'29.31" W	53.4	4.08	8.2	4.3
Mirador	VM15- B2	1979 CE	Bomb	40°21'36.61" S, 72°03'29.31" W	53	4.15	8.3	4.3
Mirador[b]	VTL-30	1979 CE	Lapilli	40°21'39.97" S, 72°03'36.41" W	51.6	4.23	7.78	4.2
Mirador[b]	VTL-31	1979 CE	Lava	40°21'44.04" S, 72°03'31.23" W	50.8	4.14	7.64	4.3

[a] ages from Bucchi et al. [2015]
[b] whole rock data from Chamberlain et al. [2024]

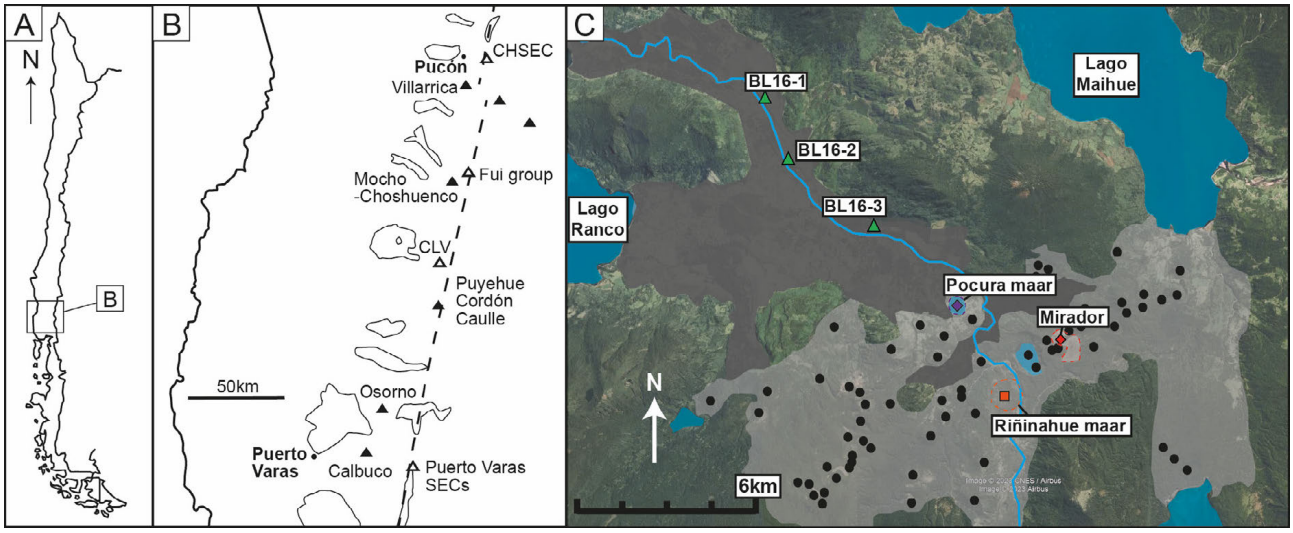

Figure 1: Location of the Carrán-Los Venados volcanic field in Southern Chile. [A] Location of the lakes region of Southern Chile. [B] Schematic map of the lakes region showing stratovolcanoes and small eruptive centres (SECs) referred to here. Dashed line is the approximate trace of the Liquiñe Ofqui Fault Zone. [C] The Carrán-Los Venados Volcanic Field (base map from Google Earth), with overlays of the approximate extent of the Basal Lavas (dark grey) and the Holocene field of small eruptive centres (light grey, known vents are shown as black circles). The locations of the three Basal Lava (BL16-1 to 3), Pocura Maar, Mirador volcano and Riñinahue maar samples are marked (see Table 1 for locations). Extent of deposits modified from Bucchi et al. [2015].

3.3 Whole rock Sr-Nd-Pb and U-Th isotopes

3.3.1 *Sr-Nd-Pb isotopes*

Thirteen samples were prepared and analysed for Sr-Nd-Pb isotopes at the Arthur Holmes Laboratory in the Department of Earth Sciences at Durham University by multi-Collector ICP mass spectrometry (MC-ICP-MS) using a ThermoFisher Neptune. These samples were selected from the 38 collected samples to represent the range in eruptive styles and relative age. The 8 samples from the Holocene tephras come from all sampled locations (see Table 1, 3 out of the 4 Basal Lavas were selected, and the stratigraphically lowest tephra sample and most proximal lava sample were selected from Mirador as being closest to the earliest and latest eruptive products as possible. Approximately 100 mg of sample powder was leached in 6 M HCl for 60 minutes on a hotplate at 100 °C before the HCl was decanted and the remaining residue rinsed with MQ H_2O. The sample was then dissolved with 1 mL ~15 M HNO_3 plus 3 mL ~29 M HF in a sealed beaker on a hotplate at 140 °C. Following sample dry down 15 M HNO_3 was added to the residue to remove fluorides before being dissolved in 3 M HNO_3 ready for column processing. Samples were initially passed through Sr Spec resin columns following the procedure outlined in Font et al. [2008] with Sr being collected in 18.2 MΩ H_2O and Pb being collected in 8 M HCl. The initial waste eluant from the Sr columns contains the REE fraction and this was passed through a cation resin column to remove other matrix elements from the REE fraction following the procedure outlined in Dowall et al. [2003]. Following column chemistry the Sr, Nd and Pb fractions were dried down, organics oxidised with a concentrated HNO_3 – 30 % H_2O_2 dry down and taken up in 3 % HNO_3 for analysis.

Sr isotopes were measured on the Neptune MC-ICP-MS in wet plasma mode. Instrumental mass bias was corrected for using a $^{88}Sr/^{86}Sr$ ratio of 8.375209 (the reciprocal of the $^{86}Sr/^{88}Sr$ ratio of 0.1194) and an exponential law. Measured Sr data were normalized to a NBS987 value of 0.710240, with NBS987 being analysed every 5 samples. The accuracy and reproducibility on NBS987 for the analytical session was excellent with an average value for NBS987 and reproducibility 0.710239 ± 0.0000016 (22.5 ppm 2SD, n = 9). Two repeat analyses of 3 samples (repeat leaching and digestion) yielded $^{87}Sr/^{86}Sr$ within 11 ppm. BHVO-1 (leached) processed alongside the samples was yielded a Sr isotope composition of 0.703464 ± 0.000010 (2SE), within 5 ppm of the value reported in Weis et al. [2006].

Nd isotopes were measured on the Neptune MC-ICP-MS in wet plasma mode with the identical sample introduction set up. Instrumental mass bias was corrected for using a spiked $^{146}Nd/^{145}Nd$ ratio of 2.079143 (equivalent to the more commonly used $^{146}Nd/^{145}Nd$ ratio of 0.7219) and an exponential law. The internal isotope reference standard J&M was run both pure and doped with Sm (Sm/Nd~0.25) to assess accuracy of the Sm correction. The average value and reproducibility for both pure and doped J&M for the analytical session was 0.511114 ± 0.000010 (20 ppm 2SD, n = 13). Sample Nd data are normalized relative to a J&M value of 0.511110 (with J&M being run every 5 samples), which is equivalent to the La Jolla value of 0.511862. Sample measurements yielded an average Sm/Nd ratio of 0.25 ± 0.046 (2SD), almost identical to the doped J&M standard. Differences between repeat analyses on the 3 samples, as detailed above for Sr, were between 6 and 2 ppm, which is very similar to the reproducibility on the J&M standard. The Nd isotope composition of BHVO-1

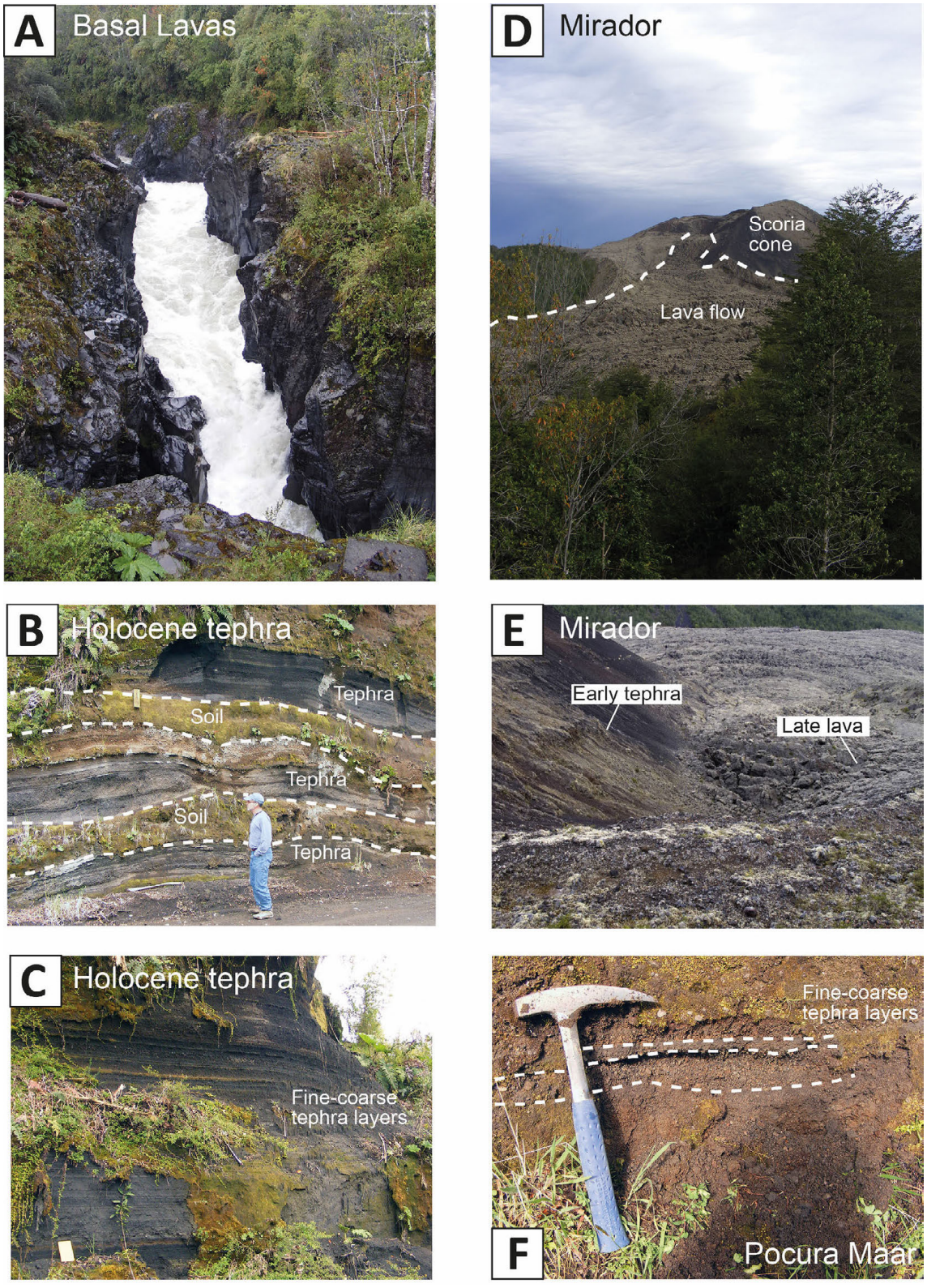

Figure 2: Field photographs of the studied volcanic products. [A] Basal lavas at Paso de la Mula, where sample BL16-3 was collected. [B] Interbedded soils and tephra at the site of samples UF17-6 to 8. [C] Long sequence of tephra fall with little soil at site of samples UF17-9 to 13. [D] View of the Mirador scoria cone and lava flow, looking northwest from the road. [E] View southeast down into the source of the lava, showing locations of samples VM15-8 (latest lava sampled) and VM15-9 (earliest tephra sampled). [F] Tephra layers in roadcut above Pocura Maar (PM16-2 and -3).

which was leached and processed alongside the samples was measured as 0.512982 ± 0.000006, 2 ppm off the value given by Weis et al. [2006] and with a measured Sm/Nd ratio of 0.259 showing the excellent accuracy of the Sm correction on real samples.

Pb isotopes were measured on the Neptune in wet plasma mode using the same introduction set up as for Sr and Nd. As Pb only has one stable non-radiogenic isotope (^{204}Pb), thallium was used to correct Pb isotope ratios for the effects of instrumental mass bias. Repeat analyses (n = 11) of the international reference material NBS981 during the analytical session gave the following average values: $^{206}Pb/^{204}Pb$ = 16.94153 ± 0.0011 (67 ppm 2SD), $^{207}Pb/^{204}Pb$ = 15.4990 ± 0.0006 (41 ppm 2SD) and $^{208}Pb/^{204}Pb$ = 36.7189 ± 0.0011 (30.2 ppm 2SD) in good agreement with accepted values of 16.9416, 15.4999 and 36.7258 from Baker et al. [2004]. Sr-Nd-Pb isotope data are presented in Table 2, all standard measurements can be found in Supplementary Material 1 Sheet 2 and expanded method details are in Supplementary Material 2.

3.3.2 *U-Th isotopes*

U and Th isotopic ratios on bulk rock powders for 11 samples were obtained at Macquarie GeoAnalytical (MQGA) at Macquarie University. All samples analysed were those for which Sr-Nd-Pb isotopes were also obtained, with the omission of 2 tephras due to column space requirements. Approximately 0.3 g of powdered rock was spiked with ^{236}U-^{229}Th and digested in concentrated acids (HF-HNO_3). Separation of U and Th followed standard anionic resin chromatography as described in Turner et al. [2011]. Uranium and thorium concentrations and U-Th isotope ratios were measured separately in static mode on a Nu Instrument Multi-Collector ICP-MS at Macquarie University. The New Brunswick Laboratory (NBL) synthetic standards U010 and U005a were used at regular intervals to assess the robustness of instrumental corrections and to monitor drift. Th concentration and ratio determinations used a standard-sample bracketing procedure using the Open University Th 'U' standard solution, and a linear tail correction for the ^{232}Th tail on ^{230}Th was applied. ($^{234}U/^{238}U$) ratios for all samples and standards were all 1.000 ± 0.006 (and mostly ± 0.003 or less) with the exception of Basal Lava sample FB091012-7 which was measured as 1.015. The USGS rock standard BCR-2 was processed with the samples in two analytical sessions (two digestions each measured twice) with the following average ratios ($^{230}Th/^{232}Th$) = 0.875 ± 0.005, and ($^{238}U/232Th$) = 0.879 ± 0.014 which are in excellent agreement with values published in Scott et al. [2019] (($^{230}Th/^{232}Th$) = 0.879 ± 0.005, ($^{238}U/^{232}Th$) = 0.877 ± 0.015). Two digestions of the standard TML (Table Mountain Latite) were analysed and gave the average ratios ($^{230}Th/^{232}Th$) = 1.072 ± 0.006 and ($^{238}U/^{232}Th$) = 1.074 ± 0.017 which are also in excellent agreement with values published in Scott et al. [2019] (($^{230}Th/^{232}Th$) = 1.077 ± 0.006, ($^{238}U/^{232}Th$) = 1.073 ± 0.045). All U-series data are presented in Table 2, and all standard measurements can be found in Supplementary Material 1 Sheet 3.

Table 2: Whole rock isotope data for all samples from the Carrán Los Venados region. All volcanic centres and sample numbers refer to those in Table 1. Full major and trace element concentrations are available in Supplementary Material 1.

Volcanic Centre	Basal lavas	Basal lavas	Basal lavas	Holocene tephras	Holocene tephras	Holocene tephras	Holocene tephras	Holocene tephras	Holocene tephras	Holocene lava	Mirador tephra
Sample Number	BL16- 2	BL16- 3	FB091012-7	UM17- 1	UF17- 2	UF17- 4	UF17- 6	UF17- 7	UF17- 10	UF17- 13a	UF17- 14a	VM15- 8	VM15- 9
$^{87}Sr/^{86}Sr$	0.70406	0.704051	0.70408	0.704073	0.704116	0.704075	0.704061	0.703988	0.704188	0.704100	0.70412	0.70407	0.70409
2SD	0.00001	0.000009	0.00001	0.000009	0.000009	0.000009	0.000012	0.00001	0.000011	0.000009	0.00001	0.00001	0.00001
$^{143}Nd/^{144}Nd$	0.512875	0.51288	0.512860	0.512868	0.512868	0.512865	0.512859	0.512867	0.512882	0.512864	0.512866	0.512864	0.512869
2SD	0.000008	0.000006	0.000005	0.000006	0.000007	0.000005	0.000005	0.000006	0.000007	0.000005	0.000006	0.000006	0.000005
U (ppm)	0.739	1.07	0.748		0.207	0.237	0.187	0.221	0.184	0.185		0.235	0.235
AE	0.008	0.01	0.008		0.002	0.003	0.002	0.002	0.002	0.002		0.008	0.008
Th (ppm)	2.61	3.77	2.7		0.526	0.676	0.534	0.724	0.517	0.473		0.675	0.675
AE	0.03	0.04	0.03		0.006	0.008	0.006	0.008	0.006	0.005		0.003	0.003
$(^{234}U/^{238}U)$	1.006	0.998	1.015		1.001	1.002	1	0.999	1	1		1.003	1.004
2SD	0.004	0.004	0.004		0.004	0.004	0.004	0.004	0.004	0.004		0.004	0.004
$(^{238}U/^{232}Th)$	0.859	0.857	0.84		1.194	1.061	1.062	0.924	1.077	1.185		1.058	1.055
2SD	0.014	0.014	0.014		0.019	0.017	0.017	0.015	0.017	0.019		0.017	0.017
$(^{230}Th/^{232}Th)$	0.807	0.817	0.805		0.845	0.853	0.892	0.867	0.839	0.852		0.823	0.825
2SD	0.005	0.005	0.005		0.005	0.005	0.005	0.005	0.005	0.005		0.005	0.005
$(^{238}U/^{230}Th)$	1.065	1.049	1.043		1.412	1.244	1.19	1.066	1.284	1.391		1.286	1.279
2SD	0.017	0.017	0.017		0.023	0.02	0.019	0.017	0.02	0.022		0.021	0.02

Note: "2SD" is 2 × standard deviation and "AE" is absolute error.

3.4 Microprobe data

In situ major and minor element data was collected on 10 thin sections representing all stages of the CLV volcanism: 1 from the Basal Lavas, 4 from Holocene tephras, 1 from Pocura Maar, 1 from Riñinahue and 3 samples of Mirador including the earliest sampled tephra and latest erupted lava collected. Major element data were collected by wavelength dispersive spectrometry on a JEOL JXA-8230 Superprobe Electron Probe Microanalyzers at the University of Iowa and the University of Leeds (data are in Supplementary Material 1 Sheet 4). Analytical conditions varied depending on the phase being analysed: all analyses were conducted using a 30 nA beam current, an accelerating voltage of 15–20 keV, beam size of either 1 or 5 µm, and on peak count times of 10–130 s. For full details of analytical conditions and associated precision and accuracy see Burney et al. [2020] for data collected at the University of Iowa and Chamberlain et al. [2024] for data collected at the University of Leeds.

Following *in situ* analyses, magmatic temperatures were modelled from measured olivine compositions and whole rock (assumed here to represent melt compositions, due to microcrystalline nature of the groundmass preventing analysis of melt composition). For the olivine-melt thermometry (following Putirka et al. [2007] equation 4), equilibrium between 'melt' (in this case, whole rock compositions) and olivine minerals was tested; any analyses where K_D(Fe-Mg)ol-liq ≠ 0.3 (± 0.03) were not used [Putirka et al. 2007].

4 Results

4.1 Petrography and mineral compositions

Studies of thin sections reveal differences in mineral modes and compositions between the Basal Lavas and subsequent younger eruptive products. The Basal Lava Riñinahue (BL16-2) has a glassy groundmass with microlites of acicular plagioclase and magnetite. The primary macrocryst (> 1 mm) phase is plagioclase, which is up to 2 mm in length and generally euhedral (Figure 3A). The olivine in the Basal Lava is subhedral to anhedral with thin rims of microgranular clinopyroxene and has forsterite (Fo) proportions between 0.60 and 0.71 with normal zoning (Figure 4A–B), and Ni concentrations of 0 to 915 ppm (Figure 4B). Plagioclase crystals have compositions between $An_{41}Ab_{56}Or_3$ and $An_{57}Ab_{41}Or_1$ with small differences between core and rim (Figure 4C).

Holocene tephra samples UF17-7 and UF17-10, (Figure 3C–D) have a glassy groundmass with microlites of plagioclase olivine and opaque phases. These samples also have crystal clots up to 3 mm in length of clinopyroxene and plagioclase , as well as variably melted granitic xenoliths present in both samples studied here. Olivines in a single microglomerocryst (total width < 300 µm) have compositions like those of Basal Lavas (Figure 4B). Most olivine crystals from Holocene tephras have distinctly higher Fo proportions (Fo = 0.7–0.8) and extend to higher Ni concentrations (up to 1547 ppm) compared with the Basal Lavas (Figure 4A–B). Plagioclase range from $An_{57}Ab_{43}$ and $An_{83}Ab_{17}$ with no difference between core and rim analyses (Figure 4C). Plagioclase microlites are stubby and show no evidence for the rapid growth that caused the acicular morphology of plagioclase in the Basal Lavas. Where oxides were large enough to analyse (see Supplementary Material 1 Sheet 4), data indicates magnetite as the sole oxide phase in the Holocene fall studied. Contrastingly, the Pocura Maar (PM16-1) sample is entirely crystalline or nearly so, with a coarse groundmass of tabular plagioclase, clinopyroxene and olivine (up to 0.5 mm), rare <1 %) feldspar macrocrysts up to 1 mm in length are present (Figure 3B). The olivines have unusually low Fo contents (0.48–0.57) and Ni concentrations of <82 ppm (Figure 4A–B) with little difference between core and rim. None of these olivines are in equilibrium with the whole rock compositions (Figure 4A). The Pocura Maar plagioclase core compositions are comparable to those from Holocene tephra and Mirador cores with compositions varying mainly between $An_{62}Ab_{37}Or_1$ and $An_{74}Ab_{26}$ Figure 4C, whereas Pocura Maar rims are similar to Mirador rims and Basal Lava plagioclase compositions and have a more restricted range of $An_{43}Ab_{55}Or_2$ to $An_{47}Ab_{51}Or_2$ (Figure 4C).

The historic Volcán Mirador and Volcán Riñinahue samples (VM15-9, VM15-13 and VTL-29) all preserve interstitial glass, with acicular plagioclase and hopper morphology olivine microlites and minor skeletal exsolved oxides. The largest mineral phases are up to 1 mm in length and are plagioclase or olivine. Rare clinopyroxene is present in the groundmass assemblage (Figure 3E–F). Olivines have restricted Fo and Ni concentrations which overlap with the lower ranges for the Holocene tephra deposits (Figure 4B). There is no difference between olivine compositions from the tephra and lava samples from Volcán Mirador, with both showing Fo 0.60 to 0.73 with normal zoning (Figure 4A) and Ni from below detection limit to 212 ppm (Figure 4B). Plagioclase compositions (obtained for Mirador only) display the same core-rim variation within a similar range as Pocura Maar, from $An_{63}Ab_{35}Or_2$ to $An_{73}Ab_{27}$ for the cores and $An_{43}Ab_{55}Or_1$ to $An_{65}Ab_{35}$ for the rims Figure 4C. In contrast to the Holocene tephras, oxides from Mirador and Riñinahue are dominantly high-Fe titanomagnetite, with a single ilmenite grain analysis (Supplementary Material 1 Sheet 4). Oxides commonly have skeletal habits with some evidence of exsolution lamellae. Mirador tephras and bombs in the field contained rare fragments up to 8 cm in length of partially melted granitoids; these were not observed in thin section however.

4.2 Whole rock major and trace element compositions

Major element compositions (Figure 5) are relatively restricted for all samples, with SiO_2 concentrations varying from 51 to 56 wt.% and MgO from 3 to 6 wt.%. Samples are all basalt to basaltic andesite, with three Basal Lava samples overlapping with the field for trachy-basalt (Figure 5A). The Basal Lava samples have elevated $Fe_2O_3{}^{tot}$, TiO_2, MnO, and particularly P_2O_5, at a given MgO concentration compared to younger CLV samples. Samples from Pocura maar are the most evolved in terms of SiO_2, MgO and total alkalis, and form an end member for the Holocene tephras (Figure 5). Al_2O_3 concentrations have three tiers, with Mirador and some Holocene tephras having the highest Al_2O_3, other Holocene tephras and the Pocura maar samples having intermediate concentrations, and Basal Lavas having the lowest concentra-

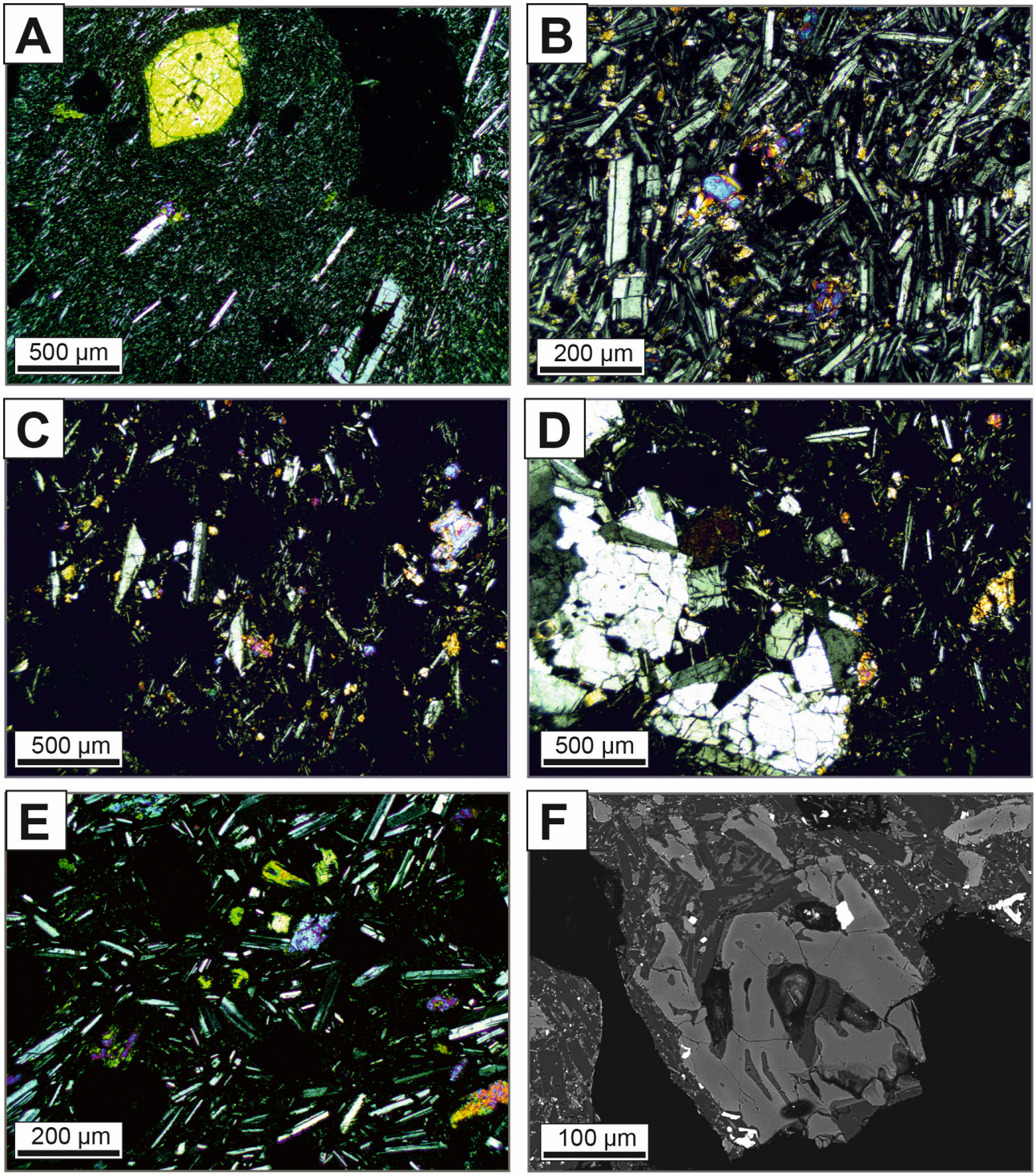

Figure 3: Representative mineral textures from Carrán Los Venados samples, all taken on an optical microscope in cross polarised light, except [F] as a back scattered electron (BSE) image from a SEM. [A]: Basal lavas showing fine grained groundmass and macrocrystic pyroxene; [B] Pocura Maar bomb with macroscopic groundmass dominated by plagioclase with minor olivine; [C] Holocene tephra clasts with glassy groundmass and increased vesicularity; [D] Holocene tephra with large granitic xenolith; [E] Mirador scoria with skeletal (hopper) olivine microphenocrysts and acicular feldspars; [F] BSE image of Riñinahue with skeletal olivine.

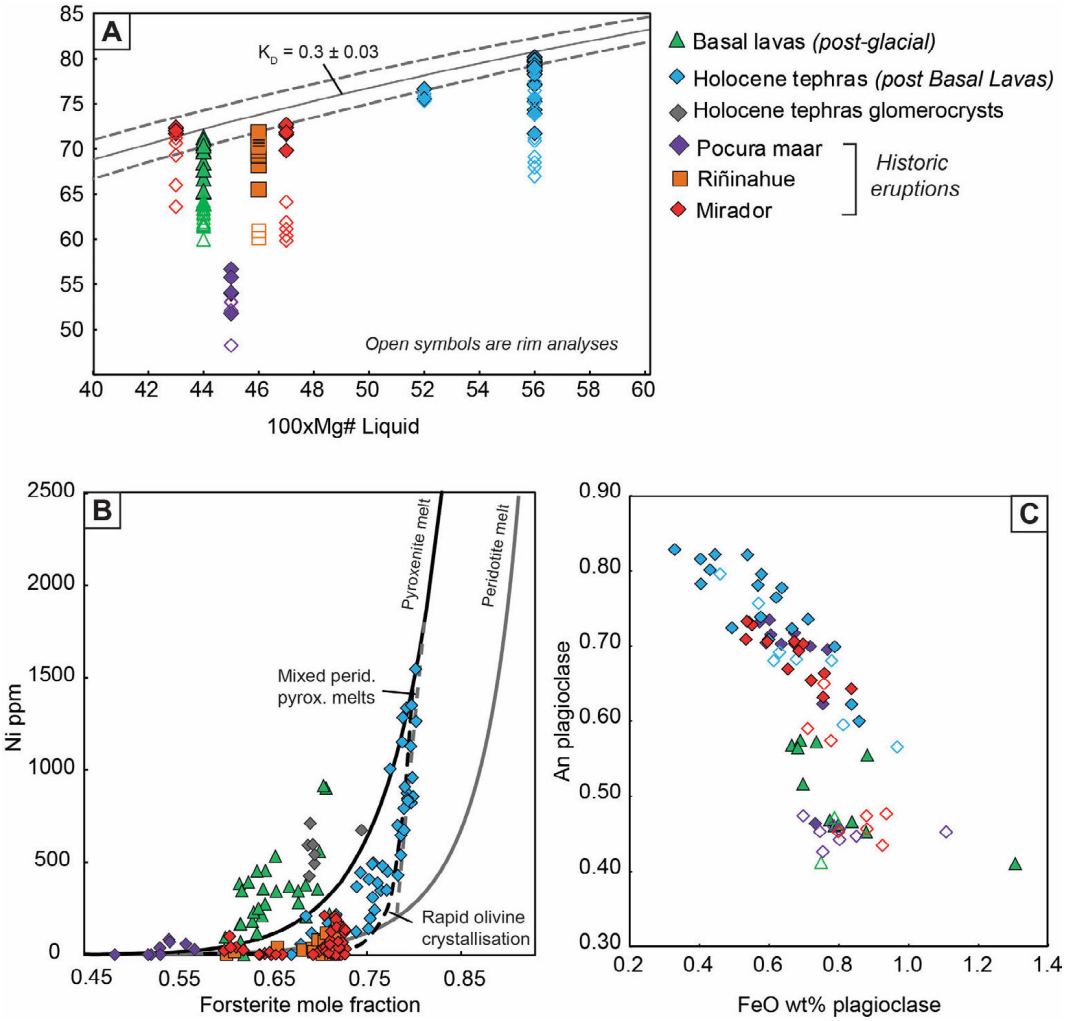

Figure 4: [A] Variation in olivine compositions with whole rock Mg# (coloured points). Lines show the calculated equilibrium compositions assuming an uncertainty of 0.03 for the Fe-Mg exchange partition coefficient (K_D) of 0.3. [B] Ni ppm vs. forsterite mole fraction in olivines from the CLV field. Model lines show crystallisation of olivine from a pyroxenite and peridotite melt after Straub et al. [2008]. The dashed black line models potential rapid crystallisation of olivine by decreasing the Ni concentration in the evolving melt to simulate rapid depletion in the melt adjacent to the crystallising olivine. An alternative explanation is the grey dashed line, which models mixing of pyroxenite and peridotite melts. [C] Anorthite vs FeO wt.% concentrations for plagioclase cores and rims analysed in this study.

tions. Samples from Mirador have narrow ranges of MgO (3.8 to 4.2 wt.%), CaO (7.6 to 8.3 wt.%), and SiO_2 concentrations (50.8 to 54.3 wt.%). Concentrations of other major elements in the Mirador samples tightly cluster. This is conspicuous on the total alkali vs. SiO_2 plot (Figure 5A) where the Holocene tephras and Pocura maar samples display a positive correlation, whereas Mirador, Riñinahue and Basal Lava samples vary primarily in SiO_2 content. The sample from Riñinahue is similar in all major elements to the Mirador samples.

On a primitive mantle-normalised [after Sun and McDonough 1989] multielement plot Nb, Ta, Zr, Hf and Ti are depleted relative to neighbouring elements U, K, Nd and Sm (Figure 6A). The Basal Lavas have high incompatible element concentrations overall compared with other samples (Figure 6A) and are notably more enriched in the rare earth elements (REE) than the other samples (Figure 6B). The samples from the Holocene tephras, Pocura maar and Mirador are more strongly enriched in most highly fluid-mobile elements (e.g. Rb, K, Ba, and Sr) compared with the Basal Lavas.

4.3 Whole rock isotopes

Sr-Nd-Pb isotopes were obtained for a subset of the Holocene tephra and Mirador samples and three Basal Lava samples. The samples from this study have a narrow range of compositions. $^{87}Sr/^{86}Sr$ varies from 0.70399 to 0.70412, $^{143}Nd/^{144}Nd$ varies from 0.512859 to 0.512882 and Pb isotopes vary from 18.581 to 18.600, 15.607 to 15.612 and 38.486 to 38.511 for $^{206}Pb/^{204}Pb$, $^{207}Pb/^{204}Pb$ and $^{208}Pb/^{204}Pb$ respectively (Figure 7). $^{87}Sr/^{86}Sr$ is high and $^{143}Nd/^{144}Nd$ is low compared with MORB, plotting with other SVZ lavas (Figure 7A), which has been attributed to a significant crustal or subducted sediment contribution. The greatest variance in our dataset (beyond uncertainties) is in Pb isotopes, with the Basal Lavas having marginally less radiogenic values compared with other

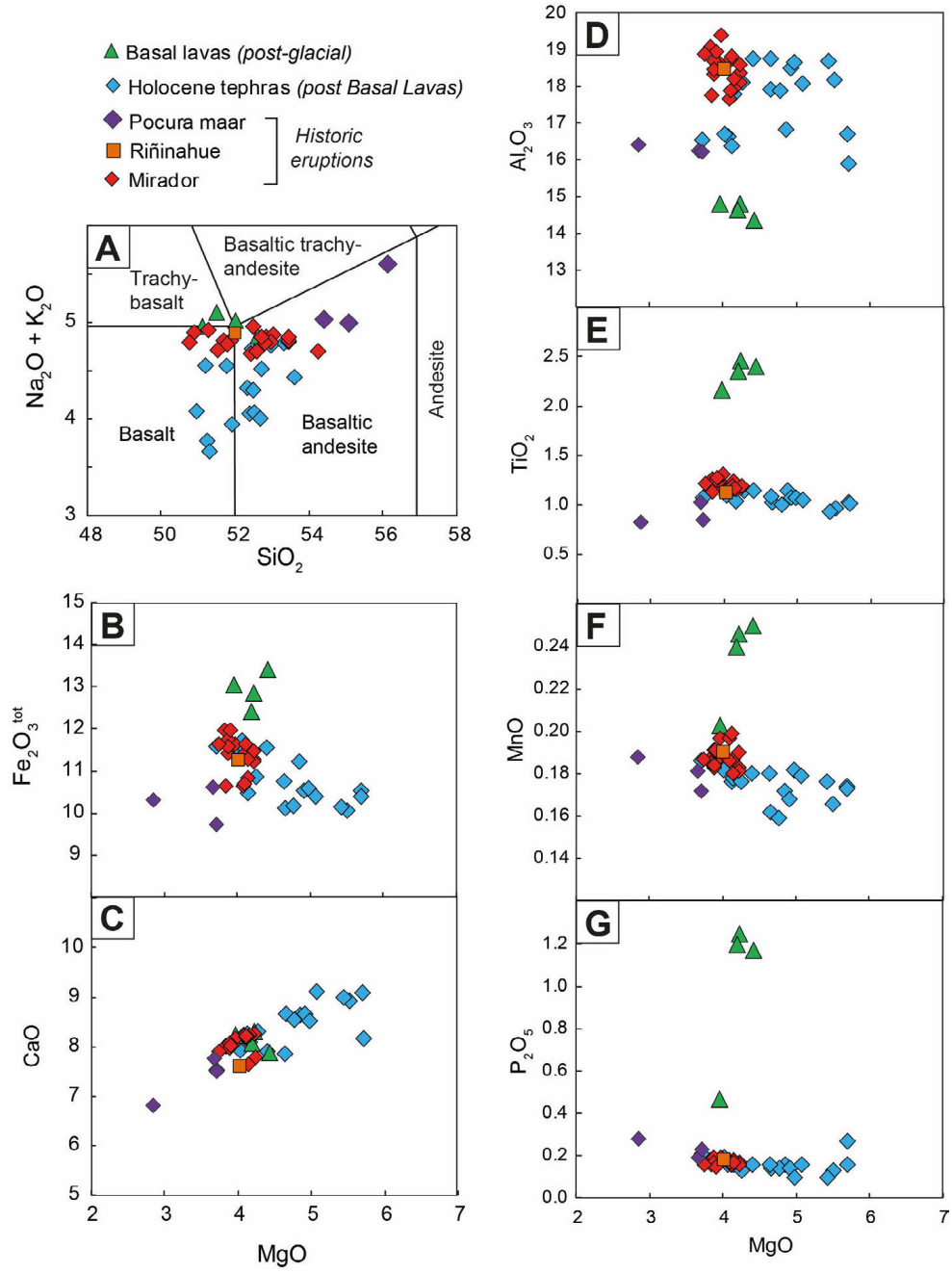

Figure 5: Whole rock major element oxides for the Basal Lavas, Holocene tephras, Pocura Maar, Riñinahue and Mirador volcanoes.

samples (Figure 7B–C) and plotting the furthest from the Chilean trench sediment field. Samples from the SVZ plot largely between the fields for MORB and Chilean trench sediment.

All samples have U-excess (i.e. $(^{238}U/^{230}Th) > 1$) ranging from 4 to 41 %, with the Holocene tephras having the greatest excesses, and the Basal Lavas plotting closest to the equiline and within the field of data for Puyehue-Cordón Caulle [from Jicha et al. 2007] (Figure 8). $(^{238}U/^{232}Th)$ varies from 0.840 to 1.185 in the Holocene tephras and Mirador samples, which extends the range of literature data for SVZ small eruptive centres (see inset to Figure 8, data from [Hickey-Vargas et al. 1989; Sigmarsson et al. 2002; Reubi et al. 2011; McGee et al. 2017; McGee et al. 2019]. $(^{230}Th/^{232}Th)$ ratios range from 0.823 to 0.892 in the Holocene tephras and Mirador samples, and the two Mirador samples (representing the earliest tephra (VM15-9) and latest lava (VM15-8), see Figure 2E) are almost identical. A sample from Mirador previously analysed by Jicha et al. [2007] has a lower $(^{238}U/^{232}Th)$ value, although $(^{230}Th/^{232}Th)$ is similar. Other samples of the most recent CLV small eruptive centres (Riñinahue and Carran) from Jicha et al. [2007] plot near the Holocene tephras analysed in this study.

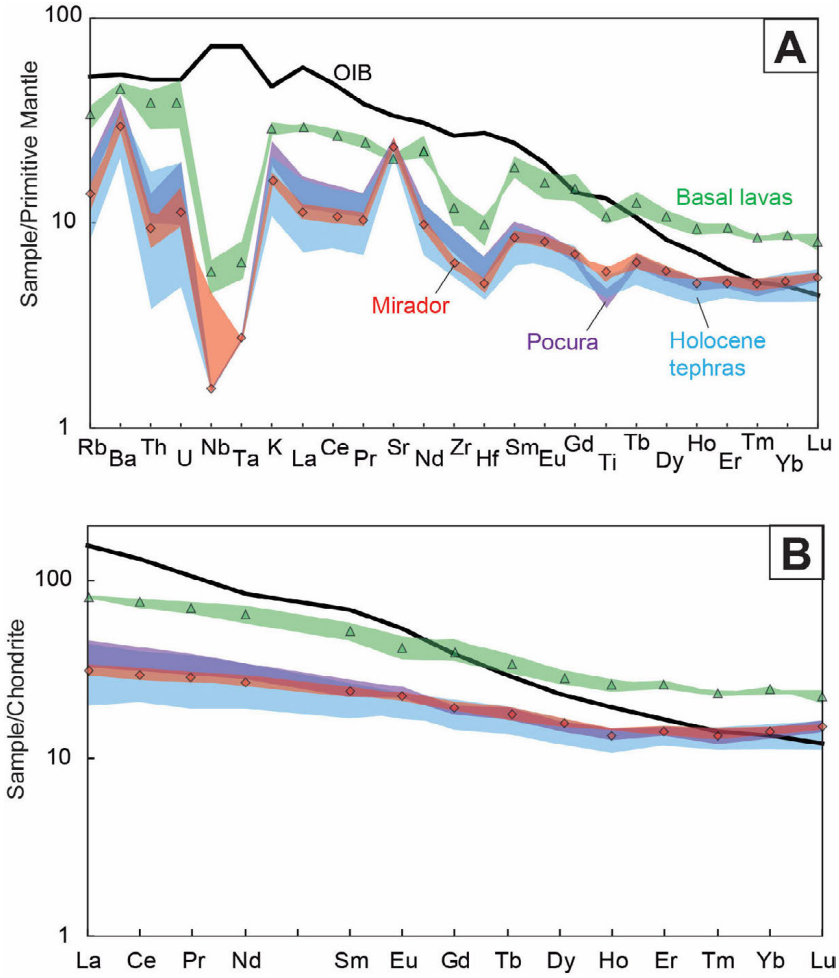

Figure 6: [A] Primitive mantle [after Sun and McDonough 1989] normalised multi element plot for all samples, plotted as fields of data. [B] Chondrite normalised [after McDonough and Sun 1995] fields of data, colours are as in A (green triangle and red diamond symbols have been added to Basal Lava and Mirador lines respectively, for easier viewing). The black line in each panel is Ocean Island Basalt from Sun and McDonough [1989].

5 Discussion

5.1 Pre-eruptive conditions from mineral chemistry

Olivine-melt thermometry (using equation 4 of Putirka et al. [2007] has been applied for analyses of cores and rims from olivine crystals in chemical equilibrium with whole rock compositions (see Section 3 and Figure 4A). Holocene tephra olivines (where both core and rim compositions can be in equilibrium with the whole rock) have the largest range in modelled magmatic temperatures, between 1127 °C and 1173 °C, outside of typical model uncertainty of ± 15 °C [Putirka 2008]. Only two olivine core analyses were within the equilibrium constraints for the Basal Lavas, and these gave temperatures of 1133 and 1137 °C, suggesting that in this case the olivine grains are not in equilibrium with their host rock, either due to assimilation of material or re-equilibration following olivine growth. Historic eruptions from Riñinahue and Mirador give lower temperatures than both the Basal Lavas and Holocene tephras, with average olivine-melt calculated temperatures of 1105 and 1098 °C respectively (from both core and rim analyses, with no difference between the modelled temperatures from core or rim analyses), suggesting that magma temperatures do not vary significantly between mineral formation and final ascent of magmas.

Fo-Ni trends in olivine from suites of lavas may be used to discriminate magmatic processes associated with olivine growth [e.g. Hart and Davis 1978; Straub et al. 2008]. For the CLV field and Basal Lavas, we modelled Fo-Ni trends for olivine crystallizing from peridotite- and pyroxenite-melts after Straub et al. [2008]. Pyroxenite melt starting compositions of 10 wt.% for MgO and 8.5 wt.% for FeO were used, and a starting olivine Ni composition of 6000 ppm [Straub et al. 2008]. The peridotite melt parental magma composition is the most primitive magma analyzed from the Puyehue-Cordón Caulle system, with 16.33 and 9.29 wt.% for MgO and FeO respectively, and 2600 ppm for the initial olivine. A Mg-Fe distribution coefficient of 0.3 [Roeder and Emslie 1970] in olivine was used, and partition coefficients for Ni in olivine were calculated by the method of Hart and Davis [1978]. Crystal fractionation was modelled numerically using 0.1 % steps (Figure 4B). Based on these models, the olivine crystals with the highest Ni concentrations from the Holocene tephras have

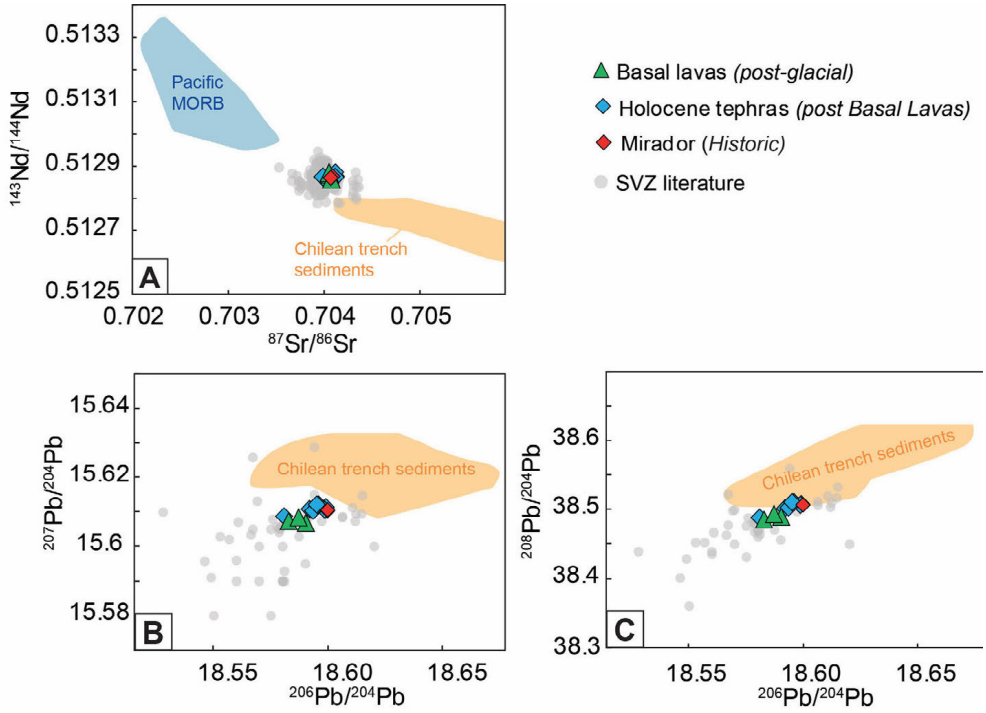

Figure 7: [A] Sr-Nd and [B–C] Pb isotopic data for the Carrán Los Venados field, compared to other SVZ volcanics [from Hickey et al. 1986; Hickey-Vargas et al. 1989; Jicha et al. 2007; Jacques et al. 2014; Morgado et al. 2015; Hickey-Vargas et al. 2016b; Turner et al. 2017; Brahm et al. 2018]. Pacific Mid Ocean Ridge Basalt (MORB, from a compilation by Stracke et al. [2003]) and Chilean trench sediments [from Kilian and Behrmann 2003; Lucassen et al. 2009] are shown for comparison. Errors are smaller than symbol size.

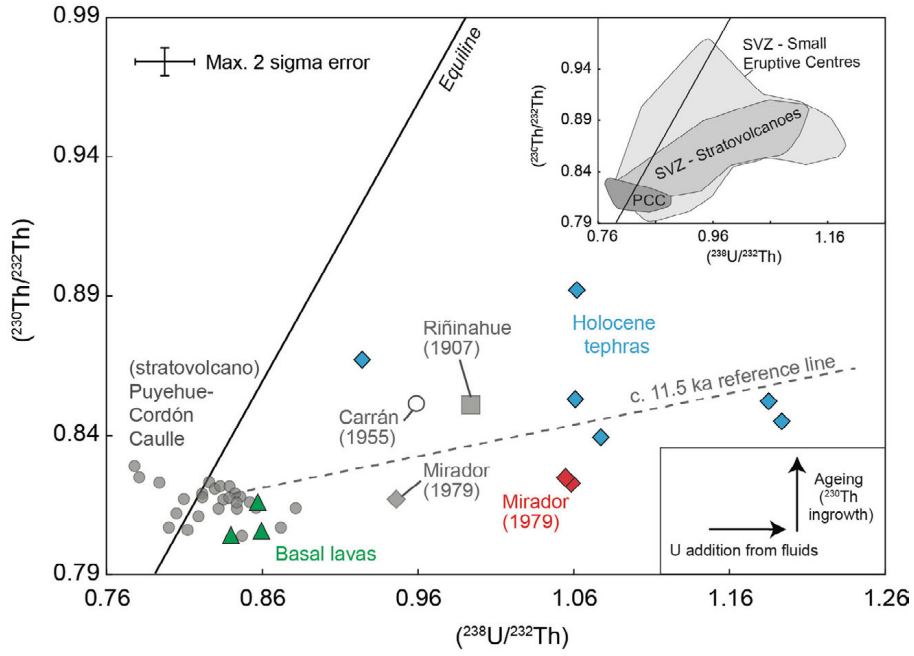

Figure 8: ($^{238}U/^{232}Th$) vs. ($^{230}Th/^{232}Th$) for the CLV field compared to previous analyses of the recent volcanics and the nearby Puyehue-Cordón Caulle stratovolcano (data from Jicha et al. [2007]). A reference line for c. 11.5 ka (the approximate timing of the deglaciation in Southern Chile) is shown. The top right inset shows literature data from SVZ small eruptive centres (Pucón and CLV) and stratovolcanoes [from Hickey-Vargas et al. 1989; Sigmarsson et al. 2002; Reubi et al. 2011; McGee et al. 2017; McGee et al. 2019].

more elevated Ni concentrations for their Fo contents than predicted by olivine fractionation from a parental peridotite melt. However, they are consistent with olivine fractionation from pyroxenite melts as was postulated for olivine Fo-Ni relationships in several volcanoes within the trans-Mexican volcanic field [Straub et al. 2008]. At that location, olivine crystals with high Ni abundances are prevalent, and it was postulated that much of the parental magma entering the crust from that field had an origin in pyroxenite generated by reaction of peridotite with silica-bearing, slab-derived melts [Straub et al. 2008].

Our data support a similar origin for some parental magmas for the Holocene tephras. However, Ni concentrations vary widely over a narrow range of Fo values for olivine crystals from the Holocene tephras. This trend could have resulted from crystallization of mixing peridotite and pyroxenite melts as illustrated in Figure 4B. An alternative explanation for the steep trend is crystal growth rates that are rapid enough to outpace Ni diffusion to the growth face because of rapid ascent to the surface accompanied by degassing from a deep magma reservoir. In this case Ni would be depleted in melts adjacent to a rapidly growing crystal as a result of the high olivine/basalt partition coefficients for Ni and Ni diffusion rates in the basaltic melts that are somewhat slower than those for Fe-Mg exchange [Gordeychik et al. 2020] and too slow to maintain equilibrium between the bulk melt and the surfaces of growing olivine (see Fig. 3 in Bacon [1989]). Decreasing the equilibrium Ni concentration by 5 % after 12 % olivine crystallisation reproduces the steep Fo-Ni trend for olivine from the Holocene tephra (black dashed line on Figure 4B).

Olivine crystals from Mirador, Riñinahue, and the Pocura maar have low Ni abundances at all Fo contents, suggesting they crystallized largely from peridotite-derived magmas and/or had previously fractionated rapidly grown olivine, consistent with hopper morphologies (Figure 3E–F). Olivine crystals from the Basal Lavas have compositions that have lower Fo concentrations than crystal fractionation trends from peridotite- or pyroxenite-derived magmas, which suggests diffusive equilibration of Fo values more than Ni in a relatively large volume, long lived magma body (see e.g. Gordeychik et al. [2020]). Further evidence of this potentially larger body is in the crystal clots found in Holocene tephras, which have olivine crystals with compositions like those in the Basal Lavas (Figure 4B).

5.2 A changing dominance of decompression melting to more fluid influenced melting

The variation in whole rock major element compositions for samples from the CLV field and Basal Lavas reveals complexities in magma source compositions, extents of melting, and differentiation processes. The variation in SiO_2 vs total alkalis across the field (Figure 5A), for example, may be explained by a difference in pressure of melt formation and/or the degree of melting of the source. Basal Lava samples have compositions that are distinct from Holocene tephras and historic eruptions. Noteworthy is the greater extent of differentiation implied by the higher concentrations of $Fe_2O_3{}^{tot}$, and TiO_2, lower concentrations of Al_2O_3, and lower Mg# for the Basal Lavas compared with Holocene tephras and historic eruptions (Figure 5).

All samples are enriched in light REE over heavy REE and REE in general over Nb, Ta, Zr and Hf, but Holocene tephras and historic eruptions have lower overall elemental concentrations (Figure 6) primarily reflecting lower degrees of differentiation. The trace element characteristics such as the pronounced depletions in Nb and Ta, the enrichments in fluid mobile elements, and the ^{238}U-excesses in all samples show that the magma sources have a significant subducted component. The subduction influence is more subdued in the Basal Lava samples, with lower ratios of fluid mobile/immobile elements such as Ba/Th and K/La compared to the rest of the field (Figure 9A–B) and with ($^{238}U/^{230}Th$) ratios closer to equilibrium (Figure 8, Figure 9A–C).

SECs from the Pucón area of southern Chile (the Caburgua-Huelemolle Small Eruptive Centres, CHSEC, Figure 1B) [Morgado et al. 2015]) have highly variable U-Th isotopic characteristics (Figure 9A-B). Those that lie close to the equiline and into the field of ^{230}Th-excess are interpreted as having a stronger decompression than fluid-flux melting signature, possibly relating to their location atop the Liquiñe-Ofqui fault system [cf. Cembrano and Lara 2009]. Those with significant ^{238}U-excesses are interpreted to result from larger inputs of subduction fluid to the source [Hickey-Vargas et al. 2016a; McGee et al. 2017; McGee et al. 2019]. Basal Lavas are close to the fields of CHSEC samples related to greater decompression melting, but still in the field of ^{238}U-excess. The Holocene tephra and historic CLV samples follow very similar trends to the CHSEC samples related to fluid-flux melting. This is consistent with trace element characteristics such as higher Ba/Th and K/La (Figure 9A–B). These observations lead to two potential hypotheses: 1) a mechanism exists whereby the subduction influence is dampened in the Basal Lavas but strengthens after their eruption or 2) a distinct mantle component present in the Basal Lavas episode is depleted before the magmatism causing the later volcanic field.

The radiogenic isotopic compositions (Figure 7), the light-enriched REE patterns (Figure 6), and relatively low Zr/Sm ratios (Figure 9C) are consistent with sources for all CLV magmas that include fluids and/or melts from subducted sediment [e.g. Plank and Langmuir 1998]. Radiogenic isotope ratios have a restricted range for all samples (Figure 7) which suggests little difference in the overall history of magma sources and that all sources include material derived from subducted sediment with a relatively homogenous composition. However, slightly elevated $^{207}Pb/^{204}Pb$ ratios that correlate with ($^{238}U/^{230}Th$) in the monogenetic field samples are consistent with an enhanced influence from subduction related fluids in the last 380,000 years compared with the Basal Lavas [e.g. Turner et al. 2003] (Figure 9F).

The similarity of the radiogenic isotope compositions argues against large-scale mantle lithological differences between the Basal Lavas and the later eruptions. However, the P_2O_5 concentrations in most Basal Lavas are anomalously high (up to 1.2 wt.%, Figure 5G), an unusual trait that is shared with some back-arc lavas from the SVZ, where the compositions were deduced to be from melting of lithospheric mantle

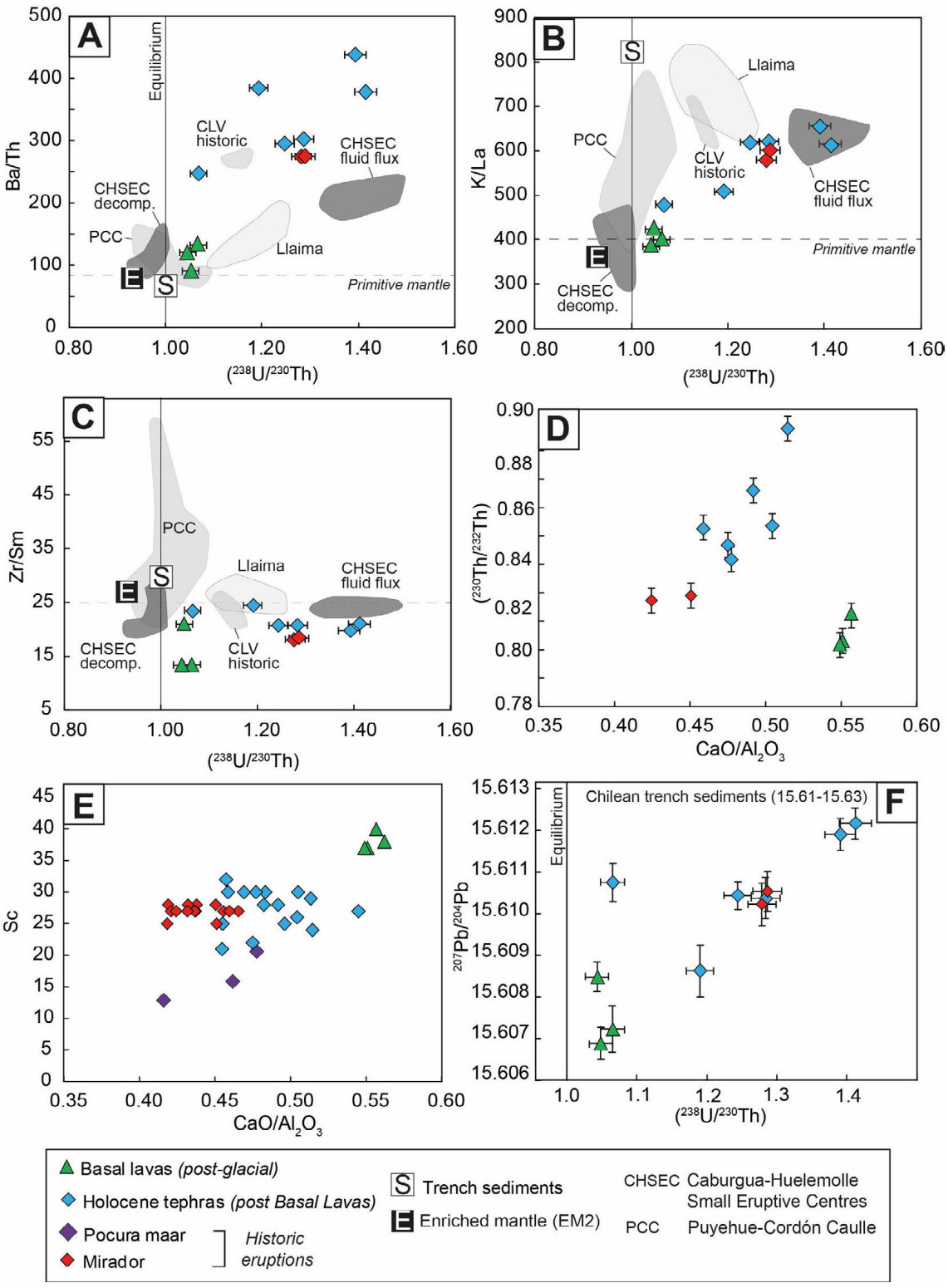

Figure 9: Isotopic and elemental variations for the CLV volcanic field compared to other stratovolcano and SEC volcanoes in the SVZ (PCC and CLV historic from Jicha et al. [2007], Llaima from Reubi et al. [2011], 'CHSEC decompression' and 'fluid flux' from McGee et al. [2017]). The horizontal dashed line in A–C is primitive mantle after Sun and McDonough [1989]. Trench sediment point (box with 'S') is from Kilian and Behrmann [2003], with the ($^{238}U/^{230}Th$) ratio assumed to be 1. Enriched mantle (box with 'E') U-Th is averaged from Samoan data in Sims and Hart [2006], and trace element ratios are averaged from Haase et al. [2019]. $^{207}Pb/^{204}Pb$ data for Chilean trench sediments in F are from the same sources as in Figure 5.

enrichments [e.g. Jacques et al. 2013]. No apatite was observed in the thin sections of the Basal Lavas. A potential explanation is its mantle source was more fertile and potentially metasomatised by subduction melts or fluids high in P and REE. Such metasomatism could be in the form of discrete domains of amphibole, apatite and/or pyroxene which were subsequently depleted, hence why the high P and REE characteristics are not observed in the later volcanic field.

Granitic micro-xenoliths are present in Holocene tephra (see Figure 3D) and partially melted granitic xenoliths up to 8cm in diameter are present in Mirador tephras. Crustal contamination could therefore play a role in the variations in magma compositions. The few Sr-Nd isotopic analyses that exist for basement rocks in Southern Chile have higher $^{87}Sr/^{86}Sr$ but significantly lower $^{143}Nd/^{144}Nd$ than the CLV volcanic samples [Davidson et al. 1987; McMillan et al. 1989; Bucchi et al. 2015] making it unlikely that crustal contamination by such basement rocks has significantly affected the minor Sr-Nd isotope variations of the CLV samples. Nevertheless, "cryptic assimilation" of material with an isotopic composition similar to that of the lavas themselves [Reagan et al. 2003; Reubi et al. 2011] cannot be ruled out, as we hypothesised for Llaima volcano (field of U-series data shown in Figure 9A–C).

5.3 Melting degree and melting rate changes over time

Due to the difference in chemical behaviours (e.g. compatibility in mineral or melt phases) in addition to the time sensitive nature of nuclides involved in the U-series decay series, U-Th ratios can be combined with major and trace element compositions to model melting degree, melting rate, and the proportion of flux versus decompression melting [e.g. Williams and Gill 1989; Lundstrom et al. 1998; Lundstrom 2003; Bourdon et al. 2005]. When the mantle is perturbed by fluid addition or upwelling it causes disequilibria in the chain of isotopes by fractionating parent and daughter isotopes. Equilibrium will be re-established within approximately five half-lives, which in the case of the U-Th part of the chain is c. 380 ka (half-life of ^{230}Th = 76 ka) (see Bourdon et al. [2003] and references therein). Thus, the fact that all samples studied here are in disequilibrium (i.e. have a $(^{238}U/^{230}Th)$ ratio > 1) means that the event or events which caused this enrichment in U occurred <380 ka. As extensive assimilation of basement would be more likely to drive the observed trend back towards the equiline, and no high U accessory phases were observed, the most likely cause of U enrichment is addition of fluids to the mantle source region within this time frame [e.g. Turner et al. 2003].

Other compositional characteristics can be used to infer information about the melting source region such as the overall trace element and isotopic composition (depleted, primitive or enriched) and modal mineralogy. The lack of ^{230}Th-excesses (Figure 8) and relatively flat middle-to-heavy REE pattern (Figure 6B) suggests a dominance of melting in the spinel-bearing rather than garnet-bearing mantle for all samples [e.g. Elkins et al. 2008], which constrains potential pressures of melting. As previously mentioned, the general similarity in the Sr-Nd-Pb isotopes (Figure 7) negates large differences in the compositions of the original mantle reservoirs and the fluids from the subducting slab. Using these inferred mantle source conditions constrained from the trace element and isotopic characteristics, modelling $(La/Yb)_N$ and $(Gd/Yb)_N$ (ratios normalised to chondrite values from Sun and McDonough [1989]) can provide insights in mantle composition and modal mineralogy (Figure 10A). Non-modal melting is assumed and modelled using melting proportions based on those in Baker et al. [1997]. These are incorporated into a modified batch melting calculation based on a bulk value for melting proportion for each element (melting proportion × K_D, summed for all minerals, in the same way that a bulk partition coefficient is calculated, after Baker et al. [1997]) (see Sheet 5 of Supplementary Material 1). This allows preferential melting of pyroxenes, fitting with the olivine model where Basal Lavas and some Holocene tephras involved pyroxenite melts (Figure 4B). A depleted MORB mantle [from Workman and Hart 2005] containing spinel was modelled for $(La/Yb)_N$ and $(Gd/Yb)_N$, but very small degrees of melting (< 1 %) are required to generate the CLV data. Turner et al. [2017] use this same mantle composition mixed with melts of EM1 compositions for their models of magma generation in the Chilean SVZ. Although adding melts of an enriched component to the depleted mantle can better simulate our dataset, this still requires the source to melt only to very small degrees before mixing. Although a large-scale involvement of depleted MORB mantle and EM1-like compositions could add to the general mantle character under this part of Southern Chile, variations in these components cannot explain the difference between the Basal Lavas and Holocene to recent eruptions at CLV.

Melting of spinel-bearing primitive mantle [Sun and McDonough 1989] fits the monogenetic field data well (Pocura, the Holocene tephras and Mirador) at realistic degrees of partial melting for small eruptive centres (3–6 %, e.g. McGee and Smith [2016]) (Figure 10A). However, although the $(La/Yb)_N$ ratios of the Basal Lavas can be modelled using this starting composition (at 3 % melting) this cannot explain their elevated $(Gd/Yb)_N$. Higher whole rock CaO/Al_2O_3 vs. Sc (Figure 9E), MnO (Figure 5F) and the relatively elevated trace element content of the Basal Lavas compared to the rest of the field (Figure 6A) suggests that their source was somewhat more enriched and fertile than the mantle source of the monogenetic CLV field. Using a source with higher modal clinopyroxene, and a starting composition with a greater enrichment in LREE and MREE to simulate the involvement of enriched fluids/melts can produce a melt which is similar to the Basal Lavas at somewhat higher degrees of melting than for the CLV field (5–7 %) (Figure 10A).

The melting parameters constrained above in a dynamic melting model based on the calculations of Williams and Gill [1989] can be used to simulate the observed $(^{230}Th/^{232}Th)$ ratios (Figure 10B). This can reveal information regarding the rate of melting across the field, as well as testing whether the degree of melting and source modes are realistic for the measured U-series isotopes. Dynamic melting differs from other melting models in that melt is continually released from melting mantle with mantle porosity (the volume percent of interstitial melt in the source before melt extraction; McKenzie

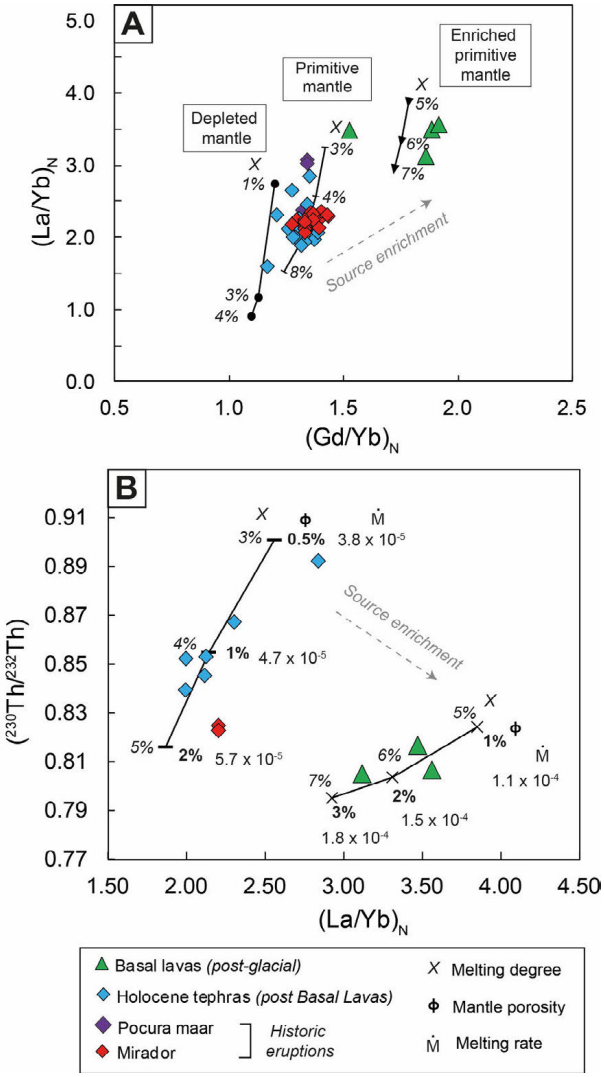

Figure 10: Melting models for the Carrán Los Venados using trace elements and (^{230}Th/^{232}Th) activity ratios. The trace element model in A constrains the potential source composition and degree of melting (X) - these are used as inputs to the model in B, which varies time-related parameters which affect the U-series isotopes (mantle porosity (ϕ), upwelling rates and melting rates) in a dynamic melting model using the models of Williams and Gill [1989]. See discussion for detail. All model parameters are given in Supplementary Material 1 Sheet 5.

[1985] and Williams and Gill [1989]) as a variable. Typical mantle porosities used in models from subduction environments are 1–5 % [e.g. Williams and Gill 1989; Turner et al. 2003; Mitchell and Asmerom 2011]. The mantle upwelling rate is an input to the model, and values of 1–5 cm yr^{-1} are considered realistic for subduction environments, based on other studies [Turner et al. 2003; Mitchell and Asmerom 2011]. Constant partition coefficients were assumed for each model iteration. It was assumed that the mantle source was in equilibrium prior to the melting event; however, by starting from a mantle source in disequilibria due to e.g. fluid-flux melting in the < 380 ka prior to the generation of the Basal Lavas, lower mantle porosities can be used in the model but other parameters are similar. It is noted that in this model the melting event is hypothesised to occur after fluid input to the mantle, rather than being directly caused by the fluid input.

Source modes used in the model in Figure 10B are those constrained in the $(La/Yb)_N$ vs. $(Gd/Yb)_N$ model (Ol 0.55: Opx 0.26: Cpx 0.15 Sp: 0.04 for the CLV field, Ol 0.46: Opx 0.25: Cpx 0.25 Sp: 0.04 for the Basal Lavas, all parameters are detailed in Sheet 5 of Supplementary Material 1). As in the trace element model enrichment was simulated in the Basal Lava source by using an increased clinopyroxene mode to simulate a more fertile source, or one which has experienced less prior mantle melting. The Basal Lava model also uses a U and Th starting concentration more enriched than primitive mantle, assuming that a LREE-MREE enriched fluid/melt would also be enriched in Th and to some extent U. Partition coefficients (K_Ds) are from Blundy and Wood [2003] except for spinel which is from Elkins et al. [2008]. Modelling the same melting conditions (i.e. degree of melting, upwelling rate, mantle porosity, melting column length) for both sources shows that the difference in composition between the hypothesised CLV field and Basal Lava sources can create the lower (^{230}Th/^{232}Th) at higher $(La/Yb)_N$ observed in the latter (Figure 10B). A difference in upwelling rate from 1 to 5 cm yr^{-1} could also explain the higher (^{230}Th/^{232}Th) in the CLV field. The model lines plotted in Figure 10B show two potential scenarios to explain the data, where the main difference is caused by the somewhat enriched mantle giving rise to the Basal Lavas, likely with higher degrees of melting and greater mantle porosity compared to the CLV field. These parameters would also mean that Basal Lava magmas are generated at a higher melting rate compared to the CLV field (as shown on Figure 10B). The reasons for these differences may be linked to the environment of melt generation.

5.4 A temporally constrained change in melting regime

Two potential scenarios were put forward to explain the difference between the inter- to postglacial Basal Lavas and the younger volcanic field: 1) A dampened subduction influence in the Basal Lavas and 2) melting of a component in the Basal Lavas episode which is less present in the volcanic field. Based on the above discussion it appears that both scenarios are likely correct. We do see evidence of a P-rich metasomatic component involved to a greater extent in the genesis of the Basal Lavas that is less significant in the generation of the volcanic field magmas. There is also the suggestion from olivine Fo-Ni trends that more pyroxenitic mantle melts were involved in the generation of the Basal Lavas and some of the Holocene tephras. The Sr-Nd-Pb isotopic data, however, do not suggest large scale lithological differences in the history of the mantle source regions. Similarly, from olivine compositional data, no significant differences can be seen in magmatic temperatures between the Basal Lavas and the later Holocene monogenetic field, and all magmas were hydrous. Rare occurrences of whole, non-disaggregated granitic xenoliths in the Mirador tephra and one Holocene Tephra sample do not provide significant evidence for assimilation of pre-Andean crust in any magma, which is corroborated by the isotopic data as previously stated. There is strong evidence

that the magmas generating the Holocene field had a more significant influence from subduction related aqueous fluids than the Basal Lavas, mainly in the significantly higher U-excess, higher fluid mobile/immobile element ratios, and correlation between $^{207}Pb/^{204}Pb$ and ($^{238}U/^{230}$ Th) (Figure 8, Figure 9F). This fluid was less prominent in the genesis of the Basal Lavas, and the U-series modelling indicates a greater dominance of decompression driven melting.

A mechanism is therefore required whereby the melting regime changes between the eruption of the Basal Lavas and the genesis of magmas that erupt as the SECs in the field. The strongest contender for this, bearing in mind that the subduction characteristics have not changed in this timeframe, is deglaciation [e.g. Huybers and Langmuir 2009]. Volcanic flare-ups at stratovolcanoes in the SVZ such as Mocho-Choshuenco [Rawson et al. 2016] and in other arcs globally [e.g. Singer et al. 2024] have been linked to the last deglaciation. The majority of research into ice loading and unloading and the effect this has on mantle melting dynamics have focussed on Iceland, where eruption rates can be correlated to glacial cycles and are shown to be substantially higher at the end of glacial cycles [e.g. Jull and McKenzie 1996; Maclennan et al. 2002]. Although mantle melting in this environment is decompression-driven, unloading of 2 km of ice over 1000 years was calculated to increase melting rates by 30 times, and this was reflected in the geochemistry of the resultant lavas, having signatures indicative of larger degrees of melting [Jull and McKenzie 1996]. This has also been noted in individual Icelandic examples (Snaefellsjökull, Hardarson and Fitton [1991]). In the former study, the modelled melting rate changed from 3×10^{-8} to 1.9×10^{-6} kg m^{-3} yr^{-1}. Changes in isotopic signatures linked to distinctive mantle lithologies suggest that the unloading alters the melting regime even on very short time scales (a few thousand years, Sims et al. [2013]).

The U-series data from the Carrán-Los Venados volcanic field and Basal Lavas lends support to the hypothesis that glacial unloading affects melting regimes and leads to a change in magmatic output. The data lie on a positive trend which could be interpreted as an isochron where an increase in ($^{238}U/^{232}Th$) is due to the addition of slab fluid and the increase in ($^{230}Th/^{232}Th$) is related to ageing as the system attempts to regain equilibrium by in-growth of ^{230}Th, in addition to melting affects (Figure 8 and Figure 10B). The higher ($^{230}Th/^{232}Th$) for two outliers from the Holocene tephras collected from the same succession of lapilli beds could be attributed to smaller degrees of melting (Figure 10). Whether these two points are excluded or not, the calculated time since the addition of U to the source is approximately 11 ka (or 12 ka without the outliers) which coincides with the time of Holocene deglaciation (12–7 ka, Huybers and Langmuir [2009]).

5.5 Evolution of the CLV magmatic system and its current state

Consolidating the petrographic, mineral and whole rock data across the samples presented here allows us to examine the evolution from the earlier Basal Lavas, through the Holocene tephras up until the recent, historic eruptions (Figure 11). The extensive Basal Lavas with their more differentiated whole rock compositions (Figure 5) and equilibrated olivine (Figure 4B) signify a larger, more slowly fractionating magmatic plumbing system compared with later eruptions. The magma sources for the Basal Lavas may have contained metasomatic domains giving unusual compositional characteristics (high P_2O_5, higher REE) that were absent in the sources of younger lavas (Figure 11A–B). Nevertheless, the general homogeneity in Sr-Nd-Pb isotopic compositions across the field suggests that the P-rich veins were low in abundance and transient features that did not endure long enough to significantly affect the long-lived radiogenic isotope of the bulk source. This homogeneity in isotopes also suggests that the composition of the slab sources for melts and fluids did not change significantly over time. Despite the presence of a clear subduction signal in the geochemistry of the Basal Lavas, based on U-series isotopes we suggest that decompression-driven melting dominated, potentially due to deglaciation of the region as seen by higher melting rates compared to the later field (Figure 10B).

The later monogenetic field (represented by the Holocene tephras, interpreted as multiple SECs, Figure 11C) marks a difference in melting and differentiation behaviour. Whole rock compositions are more mafic, less differentiated than the Basal Lavas, suggesting less time spent in the crust. Due to large ^{238}U-excesses and notable elevations in fluid mobile/immobile elements we suggest that fluid-flux melting dominated the melting regime. Early rapid crystal growth on ascent is indicated by Fo-Ni olivine trends (Figure 4B), the lack of large core-rim differences in plagioclase (Figure 4C) and clots of Basal Lava-like crystals reflect the remnants of a mush from the Basal Lavas. Historic eruption of small magma batches as SECs (Pocura, Mirador, Riñinahue) continued until recent times as cones and maars (Figure 11D), retaining the heavily fluid-fluxed signature seen in the Holocene tephras. Non-primitive whole rock compositions with low whole rock Ni and Cr concentrations must have involved efficient crystal-melt separation during fractional crystallisation in deeper reservoirs, also evidenced by large differences between core and rim plagioclase compositions exist. The similarity in the petrography of Mirador and Riñinahue samples, with hopper-shaped high-Ca olivines and exsolved oxides and acicular, unzoned plagioclase suggests rapid migration from a crustal (possibly transient, cf. Morgado et al. [2017]) reservoir, with limited interaction with other melt batches. The intersection of the LOFZ and NE–SW trending faults was suggested by Bucchi et al. [2015] to create some tectonic assistance of shallow magma ascent in the location of the historic eruptive centres, and this may also aid mechanical mixing or homogenisation of magmas prior to eruption. We speculate that the somewhat more evolved nature of the historic eruptions could suggest that a density barrier in the crust has been developing during the post-glacial period [e.g. Watanabe et al. 2002; Kent et al. 2010; Brenna et al. 2015], creating a cryptic filter to inhibit the ascent of more primitive magmas and encouraging more lower crustal processing before eruption than previously seen.

The historic eruptions in the CLV field give an excellent opportunity to examine the current state of the magmatic system

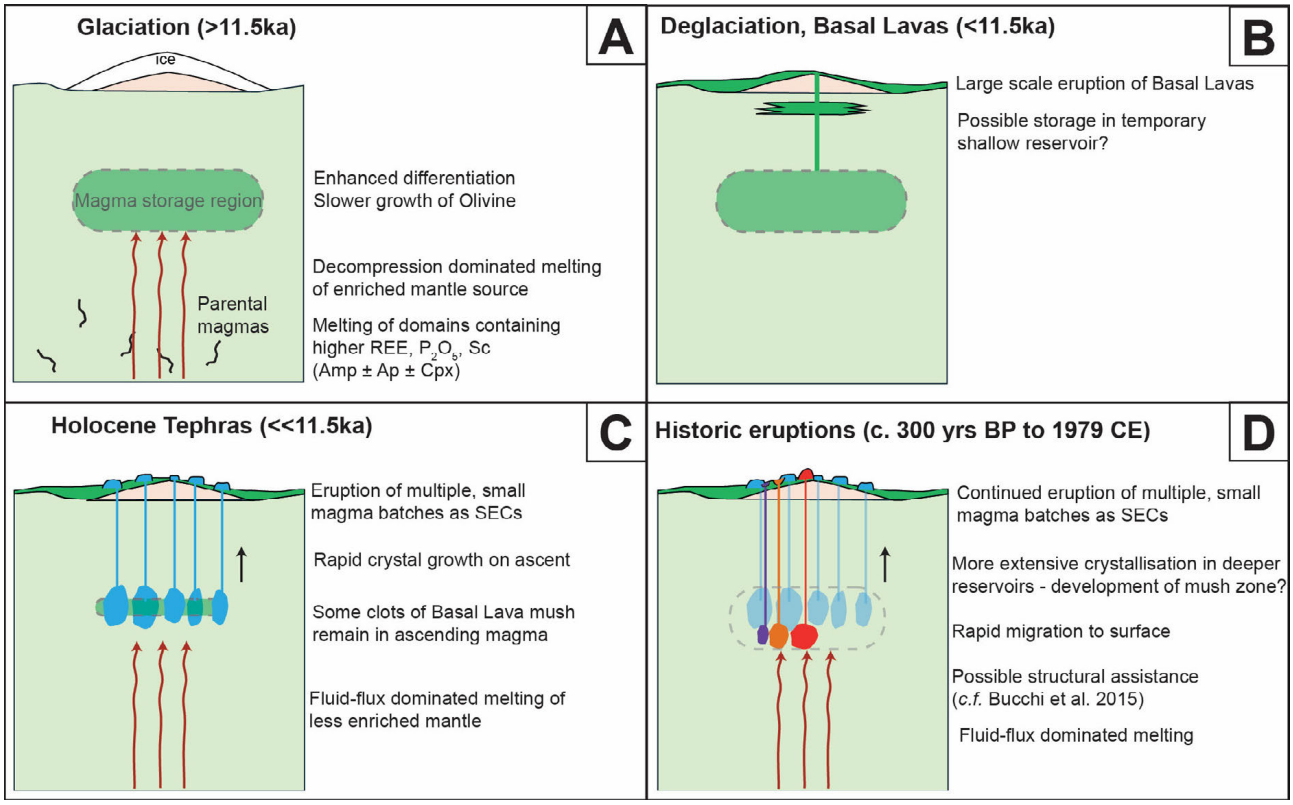

Figure 11: Schematic summary of eruption sequence hypothesised in this study, showing the change from decompression driven, larger scale eruption of the Basal Lavas followed by fluid-flux dominated small melt batches giving rise to the later Carrán-Los Venados field of small eruptive centres.

feeding the SECs, particularly as three of these centres erupted within a few decades of each other but as separate locations in the field. This frequency of eruptions, creating new cones, has not been recorded in any other historically active monogenetic fields. Basaltic small eruptive centres within Chile, and globally, show compositional variations between individual centres (e.g. the Auckland Volcanic Field of northern New Zealand [McGee et al. 2013], the Newer Volcanic Province of Victoria/South Australia [Cas et al. 2016], Jeju Island, Korea [Brenna et al. 2011], Caburgua-Huelemolle in Southern Chile [McGee et al. 2017]) highlighting the isolated nature of the melting and ascent event. Compositional variation with the progression of a single eruption has also been documented in a few cases and can reveal important detail regarding the involvement of mantle components, the changing dynamics of melting, and the evolution of crustal storage/interaction (e.g. Motukorea, Auckland, New Zealand [McGee et al. 2012], Paricutín, Mexico [Larrea et al. 2017], Jorullo, Mexico [Rasoazanamparany et al. 2016]). Samples from Mirador and Riñinahue are very similar in whole rock major and trace element compositions, and their olivine chemistry and equilibria, suggesting that on a decadal scale these eruptions are relatively homogeneous. Mirador was sampled extensively through its scoriaceous and effusive phases (see Table 1 for sample locations and Figure 2D–E). Its relatively homogeneous whole rock and isotopic composition (Figure 5 to Figure 8) shows a well-homogenised differentiated magma lacking contamination from basement rocks. Given that the most recent eruptions (Mirador and Riñinahue) have produced the most similar rock compositions in the field sampled thus far it would appear most likely that future eruptions will have similar melt generation and eruption mechanisms, with melt assembled rapidly and therefore pre-eruptive unrest is likely to be short-lived (if detected at all). In order to examine eruption trends outside of the most recent historic eruptions, detailed eruption dating campaigns of the Holocene tephra could be undertaken to connect the Holocene tephra to the historic CLV eruptions.

6 Conclusions

This study investigated the whole rock and mineral geochemistry from voluminous inter- to postglacial basaltic lava flows (Basal Lavas) and the overlying Holocene to historic Carrán-Los Venados volcanic field of monogenetic eruptive centres in Southern Chile. Some eruptions within this monogenetic field produced cinder cones, maars, and lava flows within historic times. The Basal Lavas underlying the later volcanic field have less subduction influence in the melting region, and trace element and U-series isotopic ratio models suggest somewhat larger degrees of melting and higher melting rates were involved. Olivine compositions of the Basal Lavas suggest longer storage times compared with magmas that erupted in the monogenetic field, and potential involvement of pyroxenite melts. The modelled higher melting rates may have been linked to the last deglaciation, and a change in magma productivity is seen in other volcanic centres in southern Chile with

inter- to postglacial eruptive episodes. Melting rates decreased after eruption of the Basal Lavas, although melting was more fluid-flux dominated, and smaller melt batches gave rise to small eruptive centres, seen in the higher U-excess and elevated fluid mobile/immobile ratios of the Holocene tephras and samples from Mirador (1979 CE). Homogeneous whole rock Sr-Nd-Pb isotopic data in all samples suggest that the early and late subduction components were sourced in similar lithologies. Eruption styles within the monogenetic field vary considerably. Nevertheless, historic eruption products are relatively evolved and surprisingly homogeneous in composition regardless of the sampling density (Mirador). This suggests the development of a cryptic density barrier in the crust, which may explain the limited variation in whole rock MgO, lack of primitive olivines and the relatively low concentrations of Ni and Cr.

Author Contributions

Lucy McGee: Conceptualisation, sample analysis, investigation, project administration, data curation, funding acquisition, writing - original draft and review and editing, visualisation. **Katy J. Chamberlain**: conceptualisation, sample analysis, investigation, writing - original draft and review and editing, visualisation. **Mark Reagan**: conceptualisation, sample analysis, investigation, writing - original draft and review and editing, visualisation. **Geoff Nowell**: sample analysis, writing, writing supplementary material. **Luis E. Lara**: Conceptualisation, validation, review and editing.

Acknowledgements

This project was financed by FONDECYT grant 11130296 to LM, who was supported at CEGA by FONDAP project 15090013 from 2013–2016, and a NERC Global Partnership Seedcorn Fund NE/S007520/1 to KJC. Andrea Castro is thanked for fieldwork assistance, Francisco Bucchi for the generous sharing of his knowledge of the CLV field, data and samples, Michael Turner for assistance with U-series measurements at Macquarie University, Richard Walshaw for help on the electron microprobe at the University of Leeds and Kenny Horkley for electron microprobe technical assistance to Mineralogy undergraduate students who collected data at Iowa over several years. We thank two anonymous reviewers for extremely detailed and constructive comments that greatly improved the clarity of this work, as well as editorial handling by John Browning.

Data Availability

Full datasets and methods information are available as supplementary information: Supplementary Material 1: All sample and standard data and model parameters (excel spreadsheet), Supplementary Material 2: Sr-Nd-Pb isotopes expanded methods. All whole rock elemental and isotopic data including sample locations are available at EarthChem: McGee, L. E., Chamberlain, K. J., Reagan, M. K., Nowell, G., Lara, L. E., 2025. Whole rock elemental and isotopic data for volcanic rocks from the Carran Los Venados volcanic field, Southern Chile, Version 1.0. Interdisciplinary Earth Data Alliance (IEDA). https://doi.org/10.60520/IEDA/113990.

Copyright Notice

References

Albert, H., F. Costa, and J. Martí (2016). "Years to weeks of seismic unrest and magmatic intrusions precede monogenetic eruptions". *Geology* 44(3), pages 211–214. DOI: 10.1130/g37239.1.

Ancellin, M.-A., P. Samaniego, I. Vlastélic, F. Nauret, A. Gannoun, and S. Hidalgo (2017). "Across-arc versus along-arc Sr-Nd-Pb isotope variations in the Ecuadorian volcanic arc". *Geochemistry, Geophysics, Geosystems* 18(3), pages 1163–1188. DOI: 10.1002/2016gc006679.

Bacon, C. (1989). "Crystallization of accessory phases in magmas by local saturation adjacent to phenocrysts". *Geochimica et Cosmochimica Acta* 53(5), pages 1055–1066. DOI: 10.1016/0016-7037(89)90210-x.

Baker, J., M. Menzies, M. Thirlwall, and C. MacPherson (1997). "Petrogenesis of Quaternary Intraplate Volcanism, Sana'a, Yemen: Implications for Plume-Lithosphere Interaction and Polybaric Melt Hybridization". *Journal of Petrology* 38(10), pages 1359–1390. DOI: 10.1093/petroj/38.10.1359.

Baker, J., D. Peate, T. Waight, and C. Meyzen (2004). "Pb isotopic analysis of standards and samples using a ^{207}Pb–^{204}Pb double spike and thallium to correct for mass bias with a double-focusing MC-ICP-MS". *Chemical Geology* 211(3–4), pages 275–303. DOI: 10.1016/j.chemgeo.2004.06.030.

Blundy, J. and B. Wood (2003). "Mineral-Melt Partitioning of Uranium, Thorium and Their Daughters". *Reviews in Mineralogy and Geochemistry* 52(1), pages 59–123. DOI: 10.2113/0520059.

Bourdon, B., S. Turner, G. Henderson, and C. Lundstrom (2003). "Introduction to U-series Geochemistry". *Reviews in Mineralogy and Geochemistry* 52(1), pages 1–21. DOI: 10.2113/0520001.

Bourdon, B., S. P. Turner, and N. M. Ribe (2005). "Partial melting and upwelling rates beneath the Azores from a U-series isotope perspective". *Earth and Planetary Science Letters* 239(1–2), pages 42–56. DOI: 10.1016/j.epsl.2005.08.008.

Brahm, R., M. A. Parada, E. Morgado, C. Contreras, and L. E. McGee (2018). "Origin of Holocene trachyte lavas of the Quetrupillán volcanic complex, Chile: Examples of residual melts in a rejuvenated crystalline mush reservoir". *Journal of Volcanology and Geothermal Research* 357, pages 163–176. DOI: 10.1016/j.jvolgeores.2018.04.020.

Brenna, M., S. J. Cronin, K. Németh, I. E. M. Smith, and Y. K. Sohn (2011). "The influence of magma plumbing complexity on monogenetic eruptions, Jeju Island, Korea". *Terra Nova* 23(2), pages 70–75. DOI: 10.1111/j.1365-3121.2010.00985.x.

Brenna, M., S. Nakada, D. Miura, K. Toshida, H. Ito, N. Hokanishi, and S. Nakai (2015). "A trachyte–syenite core within a basaltic nest: filtering of primitive injections by a multi-stage magma plumbing system (Oki-Dōzen, south-west Japan)". *Contributions to Mineralogy and Petrology* 170(2). DOI: 10.1007/s00410-015-1181-0.

Bucchi, F., L. E. Lara, and F. Gutiérrez (2015). "The Carrán–Los Venados volcanic field and its relationship with coeval and nearby polygenetic volcanism in an intra-arc setting". *Journal of Volcanology and Geothermal Research* 308, pages 70–81. DOI: 10.1016/j.jvolgeores.2015.10.013.

Burney, D., D. W. Peate, M. S. Riishuus, and I. A. Ukstins (2020). "Reconstructing the plumbing system of an off-rift primitive alkaline tuya (Vatnafell, Iceland) using geothermobarometry and CSDs". *Journal of Volcanology and Geothermal Research* 399, page 106914. DOI: 10.1016/j.jvolgeores.2020.106914.

Campos, A., H. Moreno, J. Muñoz, J. Antinao, J. Clayton, and M. Martin (1998). "Area de Futrono - Lago Ranco, Region de los Lagos (1:100.000)". *Mapas Geológicos*. 8. SERNAGEOMIN.

Cañón-Tapia, E. (2016). "Reappraisal of the significance of volcanic fields". *Journal of Volcanology and Geothermal Research* 310, pages 26–38. DOI: 10.1016/j.jvolgeores.2015.11.010.

Cas, R. A. F., J. van Otterloo, T. N. Blaikie, and J. van den Hove (2016). "The dynamics of a very large intraplate continental basaltic volcanic province, the Newer Volcanics Province, SE Australia, and implications for other provinces". *Geological Society, London, Special Publications* 446(1), pages 123–172. DOI: 10.1144/sp446.8.

Cembrano, J. and L. Lara (2009). "The link between volcanism and tectonics in the southern volcanic zone of the Chilean Andes: A review". *Tectonophysics* 471(1–2), pages 96–113. DOI: 10.1016/j.tecto.2009.02.038.

Chamberlain, K. J., D. J. Morgan, L. E. Lara, R. Walshaw, J. Gardner, S. Chenery, I. L. Millar, and D. Wagner (2024). "Effect of crustal stress state on magmatic stalling and ascent: case study from Puyehue-Cordón Caulle, Chile". *Bulletin of Volcanology* 86(6). DOI: 10.1007/s00445-024-01740-w.

Condomines, M., P.-J. Gauthier, and O. Sigmarsson (2003). "Timescales of Magma Chamber Processes and Dating of Young Volcanic Rocks". *Reviews in Mineralogy and Geochemistry* 52(1), pages 125–174. DOI: 10.2113/0520125.

Davidson, J. P., M. A. Dungan, K. M. Ferguson, and M. T. Colucci (1987). "Crust-magma interactions and the evolution of arc magmas: The San Pedro–Pellado volcanic complex, southern Chilean Andes". *Geology* 15(5), page 443. DOI: 10.1130/0091-7613(1987)15<443:ciateo>2.0.co;2.

Dowall, D., G. Nowell, and D. Pearson (2003). "Chemical pre-concentration procedures for high-precision analysis of Hf/Nd/Sr isotopes in geological materials by plasma ionisation multi-collector mass spectrometry (PIMMS) techniques". *Plasma Source Mass Spectrometry: Applications and Emerging Technologies*. Edited by J. Holland and S. Tanner. Volume 288. The Royal Society of Chemistry, pages 321–337. ISBN: 978-0-85404-603-4. DOI: 10.1039/9781847551689.

Edmonds, M., K. V. Cashman, M. Holness, and M. Jackson (2019). "Architecture and dynamics of magma reservoirs". *Philosophical Transactions of the Royal Society A: Mathematical, Physical and Engineering Sciences* 377(2139), page 20180298. DOI: 10.1098/rsta.2018.0298.

Elkins, L., G. Gaetani, and K. Sims (2008). "Partitioning of U and Th during garnet pyroxenite partial melting: Constraints on the source of alkaline ocean island basalts". *Earth and Planetary Science Letters* 265(1–2), pages 270–286. DOI: 10.1016/j.epsl.2007.10.034.

Font, L., J. P. Davidson, D. G. Pearson, G. M. Nowell, D. A. Jerram, and C. J. Ottley (2008). "Sr and Pb Isotope Micro-analysis of Plagioclase Crystals from Skye Lavas: an Insight into Open-system Processes in a Flood Basalt Province". *Journal of Petrology* 49(8), pages 1449–1471. DOI: 10.1093/petrology/egn032.

Godoy, B., L. McGee, O. González-Maurel, I. Rodríguez, P. le Roux, D. Morata, and A. Menzies (2020). "Upper crustal differentiation processes and their role in ^{238}U-^{230}Th disequilibria at the San Pedro-Linzor volcanic chain (Central Andes)". *Journal of South American Earth Sciences* 102, page 102672. DOI: 10.1016/j.jsames.2020.102672.

Gordeychik, B., T. Churikova, T. Shea, A. Kronz, A. Simakin, and G. Wörner (2020). "Fo and Ni Relations in Olivine Differentiate between Crystallization and Diffusion Trends". *Journal of Petrology* 61(9). DOI: 10.1093/petrology/egaa083.

Gutiérrez, F., A. Gioncada, O. González Ferran, A. Lahsen, and R. Mazzuoli (2005). "The Hudson Volcano and surrounding monogenetic centres (Chilean Patagonia): An example of volcanism associated with ridge–trench collision environment". *Journal of Volcanology and Geothermal Research* 145(3–4), pages 207–233. DOI: 10.1016/j.jvolgeores.2005.01.014.

Haase, K. M., C. Beier, and F. Kemner (2019). "A Comparison of the Magmatic Evolution of Pacific Intraplate Volcanoes: Constraints on Melting in Mantle Plumes". *Frontiers in Earth Science* 6. DOI: 10.3389/feart.2018.00242.

Hardarson, B. S. and J. G. Fitton (1991). "Increased mantle melting beneath Snaefellsjökull volcano during Late Pleistocene deglaciation". *Nature* 353(6339), pages 62–64. DOI: 10.1038/353062a0.

Hart, S. R. and K. E. Davis (1978). "Nickel partitioning between olivine and silicate melt". *Earth and Planetary Science Letters* 40(2), pages 203–219. DOI: 10.1016/0012-821x(78)90091-2.

Hickey, R. L., F. A. Frey, D. C. Gerlach, and L. Lopez-Escobar (1986). "Multiple sources for basaltic arc rocks from the southern volcanic zone of the Andes (34°–41°S): Trace element and isotopic evidence for contributions from subducted oceanic crust, mantle, and continental crust". *Journal of Geophysical Research: Solid Earth* 91(B6), pages 5963–5983. DOI: 10.1029/jb091ib06p05963.

Hickey-Vargas, R., M. Sun, and S. Holbik (2016a). "Geochemistry of basalts from small eruptive centers near Villarrica stratovolcano, Chile: Evidence for lithospheric mantle com-

ponents in continental arc magmas". *Geochimica et Cosmochimica Acta* 185, pages 358–382. DOI: 10.1016/j.gca.2016.03.033.

Hickey-Vargas, R., S. Holbik, D. Tormey, F. A. Frey, and H. Moreno Roa (2016b). "Basaltic rocks from the Andean Southern Volcanic Zone: Insights from the comparison of along-strike and small-scale geochemical variations and their sources". *Lithos* 258–259, pages 115–132. DOI: 10.1016/j.lithos.2016.04.014.

Hickey-Vargas, R., H. M. Roa, L. L. Escobar, and F. A. Frey (1989). "Geochemical variations in Andean basaltic and silicic lavas from the Villarrica-Lanin volcanic chain (39.5°S): an evaluation of source heterogeneity, fractional crystallization and crustal assimilation". *Contributions to Mineralogy and Petrology* 103(3), pages 361–386. DOI: 10.1007/bf00402922.

Hildreth, W. and S. Moorbath (1988). "Crustal contributions to arc magmatism in the Andes of Central Chile". *Contributions to Mineralogy and Petrology* 98(4), pages 455–489. DOI: 10.1007/bf00372365.

Huybers, P. and C. Langmuir (2009). "Feedback between deglaciation, volcanism, and atmospheric CO_2". *Earth and Planetary Science Letters* 286(3–4), pages 479–491. DOI: 10.1016/j.epsl.2009.07.014.

Jacques, G., K. Hoernle, J. Gill, F. Hauff, H. Wehrmann, D. Garbe-Schönberg, P. van den Bogaard, I. Bindeman, and L. Lara (2013). "Across-arc geochemical variations in the Southern Volcanic Zone, Chile (34.5–38.0°S): Constraints on mantle wedge and slab input compositions". *Geochimica et Cosmochimica Acta* 123, pages 218–243. DOI: 10.1016/j.gca.2013.05.016.

Jacques, G., K. Hoernle, J. Gill, H. Wehrmann, I. Bindeman, and L. E. Lara (2014). "Geochemical variations in the Central Southern Volcanic Zone, Chile (38–43°S): The role of fluids in generating arc magmas". *Chemical Geology* 371, pages 27–45. DOI: 10.1016/j.chemgeo.2014.01.015.

Jankovics, M. É., T. Sági, R. L. Astbury, M. Petrelli, B. Kiss, T. Ubide, K. Németh, T. Ntaflos, and S. Harangi (2019). "Olivine major and trace element compositions coupled with spinel chemistry to unravel the magmatic systems feeding monogenetic basaltic volcanoes". *Journal of Volcanology and Geothermal Research* 369, pages 203–223. DOI: 10.1016/j.jvolgeores.2018.11.027.

Jicha, B. R., B. S. Singer, B. L. Beard, C. M. Johnson, H. Moreno-Roa, and J. A. Naranjo (2007). "Rapid magma ascent and generation of ^{230}Th excesses in the lower crust at Puyehue–Cordón Caulle, Southern Volcanic Zone, Chile". *Earth and Planetary Science Letters* 255(1–2), pages 229–242. DOI: 10.1016/j.epsl.2006.12.017.

Jull, M. and D. McKenzie (1996). "The effect of deglaciation on mantle melting beneath Iceland". *Journal of Geophysical Research: Solid Earth* 101(B10), pages 21815–21828. DOI: 10.1029/96jb01308.

Kent, A. J. R., C. Darr, A. M. Koleszar, M. J. Salisbury, and K. M. Cooper (2010). "Preferential eruption of andesitic magmas through recharge filtering". *Nature Geoscience* 3(9), pages 631–636. DOI: 10.1038/ngeo924.

Kilian, R. and J. H. Behrmann (2003). "Geochemical constraints on the sources of Southern Chile Trench sediments and their recycling in arc magmas of the Southern Andes". *Journal of the Geological Society* 160(1), pages 57–70. DOI: 10.1144/0016-764901-143.

Lara, L. E., A. Lavenu, J. Cembrano, and C. Rodríguez (2006). "Structural controls of volcanism in transversal chains: Resheared faults and neotectonics in the Cordón Caulle–Puyehue area (40.5°S), Southern Andes". *Journal of Volcanology and Geothermal Research* 158(1–2), pages 70–86. DOI: 10.1016/j.jvolgeores.2006.04.017.

Larrea, P., S. Salinas, E. Widom, C. Siebe, and R. J. Abbitt (2017). "Compositional and volumetric development of a monogenetic lava flow field: The historical case of Paricutin (Michoacán, Mexico)". *Journal of Volcanology and Geothermal Research* 348, pages 36–48. DOI: 10.1016/j.jvolgeores.2017.10.016.

Larrea, P., E. Widom, C. Siebe, S. Salinas, and D. Kuentz (2019). "A re-interpretation of the petrogenesis of Paricutin volcano: Distinguishing crustal contamination from mantle heterogeneity". *Chemical Geology* 504, pages 66–82. DOI: 10.1016/j.chemgeo.2018.10.026.

López-Escobar, L., J. Cembrano, and H. Moreno (1995). "Geochemistry and tectonics of the Chilean Southern Andes basaltic Quaternary volcanism (37-46°S)". *Andean Geology* 22(2), pages 219–234.

López-Escobar, L. and H. Moreno (1981). "Erupcion de 1979 del Volcán Mirador, Andes del Sur, 40°21'S: Caracteristicas geoquimicas de las lavas y xenolithos graniticos". *Revista Geológica de Chile* 13-14, pages 17–33.

Lucassen, F., M. Wiedicke, and G. Franz (2009). "Complete recycling of a magmatic arc: evidence from chemical and isotopic composition of Quaternary trench sediments in Chile (36°–40°S)". *International Journal of Earth Sciences* 99(3), pages 687–701. DOI: 10.1007/s00531-008-0410-4.

Lundstrom, C. C. (2003). "Uranium-series Disequilibria in Mid-ocean Ridge Basalts: Observations and Models of Basalt Genesis". *Reviews in Mineralogy and Geochemistry* 52(1), pages 175–214. DOI: 10.2113/0520175.

Lundstrom, C., J. Gill, Q. Williams, and B. Hanan (1998). "Investigating solid mantle upwelling beneath mid-ocean ridges using U-series disequilibria. II. A local study at 33°S Mid-Atlantic Ridge". *Earth and Planetary Science Letters* 157(3–4), pages 167–181. DOI: 10.1016/s0012-821x(98)00039-9.

Maclennan, J., M. Jull, D. McKenzie, L. Slater, and K. Grönvold (2002). "The link between volcanism and deglaciation in Iceland". *Geochemistry, Geophysics, Geosystems* 3(11), pages 1–25. DOI: 10.1029/2001gc000282.

Mallea-Lillo, F., E. Morgado, L. McGee, C. Spandler, and M.-Á. Parada (2025). "From source to surface for small eruptive centres: using Sr–Nd isotopes and olivine diffusion timescales of the Fui Group (Chilean Andes)". *Contributions to Mineralogy and Petrology* 180(8). DOI: 10.1007/s00410-025-02237-1.

Mallea-Lillo, F., M. A. Parada, E. Morgado, C. Contreras, and D. Hübner (2022). "Contrasting sources and conditions of shallow magmatic reservoirs of the Fui Group small erup-

tive centres associated with the Liquiñe-Ofqui Fault Zone (Chilean Andes)". *Journal of South American Earth Sciences* 117, page 103875. DOI: 10.1016/j.jsames.2022.103875.

Mamani, M., G. Wörner, and T. Sempere (2009). "Geochemical variations in igneous rocks of the Central Andean orocline (13°S to 18°S): Tracing crustal thickening and magma generation through time and space". *Geological Society of America Bulletin* 122(1–2), pages 162–182. DOI: 10.1130/b26538.1.

McDonough, W. and S.-s. Sun (1995). "The composition of the Earth". *Chemical Geology* 120(3–4), pages 223–253. DOI: 10.1016/0009-2541(94)00140-4.

McGee, L., E. Morgado, R. Brahm, M.-Á. Parada, N. Vinet, L. E. Lara, A. Flores, M. Turner, H. Handley, and G. Nowell (2019). "Stratigraphically controlled sampling captures the onset of highly fluid-fluxed melting at San Jorge volcano, Southern Volcanic Zone, Chile". *Contributions to Mineralogy and Petrology* 174(12). DOI: 10.1007/s00410-019-1643-x.

McGee, L. E., R. Brahm, M. C. Rowe, H. K. Handley, E. Morgado, L. E. Lara, M. B. Turner, N. Vinet, M.-Á. Parada, and P. Valdivia (2017). "A geochemical approach to distinguishing competing tectono-magmatic processes preserved in small eruptive centres". *Contributions to Mineralogy and Petrology* 172(6). DOI: 10.1007/s00410-017-1360-2.

McGee, L. E., M.-A. Millet, I. E. Smith, K. Németh, and J. M. Lindsay (2012). "The inception and progression of melting in a monogenetic eruption: Motukorea Volcano, the Auckland Volcanic Field, New Zealand". *Lithos* 155, pages 360–374. DOI: 10.1016/j.lithos.2012.09.012.

McGee, L. E., I. E. M. Smith, M.-A. Millet, H. K. Handley, and J. M. Lindsay (2013). "Asthenospheric Control of Melting Processes in a Monogenetic Basaltic System: a Case Study of the Auckland Volcanic Field, New Zealand". *Journal of Petrology* 54(10), pages 2125–2153. DOI: 10.1093/petrology/egt043.

McGee, L. E. and I. E. Smith (2016). "Interpreting chemical compositions of small scale basaltic systems: A review". *Journal of Volcanology and Geothermal Research* 325, pages 45–60. DOI: 10.1016/j.jvolgeores.2016.06.007.

McKenzie, D. (1985). "230Th238U disequilibrium and the melting processes beneath ridge axes". *Earth and Planetary Science Letters* 72(2–3), pages 149–157. DOI: 10.1016/0012-821x(85)90001-9.

McMillan, N. J., R. S. Harmon, S. Moorbath, L. Lopez-Escobar, and D. F. Strong (1989). "Crustal sources involved in continental arc magmatism: A case study of volcan Mocho-Choshuenco, southern Chile". *Geology* 17(12), page 1152. DOI: 10.1130/0091-7613(1989)017<1152:csiica>2.3.co;2.

Mitchell, E. C. and Y. Asmerom (2011). "U-series isotope systematics of mafic magmas from central Oregon: Implications for fluid involvement and melting processes in the Cascade arc". *Earth and Planetary Science Letters* 312(3–4), pages 378–389. DOI: 10.1016/j.epsl.2011.09.060.

Morgado, E., M. Parada, C. Contreras, A. Castruccio, F. Gutiérrez, and L. McGee (2015). "Contrasting records from mantle to surface of Holocene lavas of two nearby arc volcanic complexes: Caburgua-Huelemolle Small Eruptive Centers and Villarrica Volcano, Southern Chile". *Journal of Volcanology and Geothermal Research* 306, pages 1–16. DOI: 10.1016/j.jvolgeores.2015.09.023.

Morgado, E., M. Parada, D. Morgan, F. Gutiérrez, A. Castruccio, and C. Contreras (2017). "Transient shallow reservoirs beneath small eruptive centres: Constraints from Mg-Fe interdiffusion in olivine". *Journal of Volcanology and Geothermal Research* 347, pages 327–336. DOI: 10.1016/j.jvolgeores.2017.10.002.

Morgado, E., D. J. Morgan, J. Harvey, A. Castruccio, R. Brahm, L. E. McGee, M.-Á. Parada, B. Georgiev, and S. J. Hammond (2022). "The Magmatic Evolution and the Regional Context of the 1835 AD Osorno Volcano Products (41°06'S, Southern Chile)". *Journal of Petrology* 63(11). DOI: 10.1093/petrology/egac105.

Németh, K. and G. Kereszturi (2015). "Monogenetic volcanism: personal views and discussion". *International Journal of Earth Sciences* 104(8), pages 2131–2146. DOI: 10.1007/s00531-015-1243-6.

Plank, T. and C. H. Langmuir (1998). "The chemical composition of subducting sediment and its consequences for the crust and mantle". *Chemical Geology* 145(3–4), pages 325–394. DOI: 10.1016/s0009-2541(97)00150-2.

Putirka, K. D. (2008). "Thermometers and Barometers for Volcanic Systems". *Reviews in Mineralogy and Geochemistry* 69(1), pages 61–120. DOI: 10.2138/rmg.2008.69.3.

Putirka, K. D., M. Perfit, F. Ryerson, and M. G. Jackson (2007). "Ambient and excess mantle temperatures, olivine thermometry, and active vs. passive upwelling". *Chemical Geology* 241(3–4), pages 177–206. DOI: 10.1016/j.chemgeo.2007.01.014.

Rasoazanamparany, C., E. Widom, C. Siebe, M.-N. Guilbaud, M. Spicuzza, J. Valley, G. Valdez, and S. Salinas (2016). "Temporal and compositional evolution of Jorullo volcano, Mexico: Implications for magmatic processes associated with a monogenetic eruption". *Chemical Geology* 434, pages 62–80. DOI: 10.1016/j.chemgeo.2016.04.004.

Rawson, H., D. M. Pyle, T. A. Mather, V. C. Smith, K. Fontijn, S. M. Lachowycz, and J. A. Naranjo (2016). "The magmatic and eruptive response of arc volcanoes to deglaciation: Insights from southern Chile". *Geology* 44(4), pages 251–254. DOI: 10.1130/g37504.1.

Reagan, M. K., K. Sims, J. Erich, R. Thomas, R. Cheng, R. Edwards, G. Layne, and L. Ball (2003). "Time-scales of Differentiation from Mafic Parents to Rhyolite in North American Continental Arcs". *Journal of Petrology* 44(9), pages 1703–1726. DOI: 10.1093/petrology/egg057.

Reubi, O., B. Bourdon, M. Dungan, J. Koornneef, D. Sellés, C. Langmuir, and S. Aciego (2011). "Assimilation of the plutonic roots of the Andean arc controls variations in U-series disequilibria at Volcan Llaima, Chile". *Earth and Planetary Science Letters* 303(1–2), pages 37–47. DOI: 10.1016/j.epsl.2010.12.018.

Roeder, P. L. and R. F. Emslie (1970). "Olivine-liquid equilibrium". *Contributions to Mineralogy and Petrology* 29(4), pages 275–289. DOI: 10.1007/bf00371276.

Ruth, D. C. S. and F. Costa (2021). "A petrological and conceptual model of Mayon volcano (Philippines) as an example of an open-vent volcano". *Bulletin of Volcanology* 83(10). DOI: 10.1007/s00445-021-01486-9.

Scott, S. R., K. W. Sims, M. K. Reagan, L. Ball, J. B. Schwieters, C. Bouman, N. S. Lloyd, C. L. Waters, J. J. Standish, and D. L. Tollstrup (2019). "The application of abundance sensitivity filters to the precise and accurate measurement of uranium series nuclides by plasma mass spectrometry". *International Journal of Mass Spectrometry* 435, pages 321–332. DOI: 10.1016/j.ijms.2018.11.011.

Sigmarsson, O., J. Chmeleff, J. Morris, and L. Lopez-Escobar (2002). "Origin of ^{226}Ra–^{230}Th disequilibria in arc lavas from southern Chile and implications for magma transfer time". *Earth and Planetary Science Letters* 196(3–4), pages 189–196. DOI: 10.1016/s0012-821x(01)00611-2.

Sims, K. and S. Hart (2006). "Comparison of Th, Sr, Nd and Pb isotopes in oceanic basalts: Implications for mantle heterogeneity and magma genesis". *Earth and Planetary Science Letters* 245(3–4), pages 743–761. DOI: 10.1016/j.epsl.2006.02.030.

Sims, K. W., J. Maclennan, J. Blichert-Toft, E. M. Mervine, J. Blusztajn, and K. Grönvold (2013). "Short length scale mantle heterogeneity beneath Iceland probed by glacial modulation of melting". *Earth and Planetary Science Letters* 379, pages 146–157. DOI: 10.1016/j.epsl.2013.07.027.

Singer, B. S., B. R. Jicha, M. A. Harper, J. A. Naranjo, L. E. Lara, and H. Moreno-Roa (2008). "Eruptive history, geochronology, and magmatic evolution of the Puyehue-Cordon Caulle volcanic complex, Chile". *Geological Society of America Bulletin* 120(5–6), pages 599–618. DOI: 10.1130/b26276.1.

Singer, B. S., P. Moreno-Yaeger, M. Townsend, C. Huber, J. Cuzzone, B. R. Edwards, M. Romero, Y. Orellana-Salazar, S. A. Marcott, R. E. Breunig, K. L. Ferrier, K. Scholz, A. N. Coonin, B. V. Alloway, M. M. Tremblay, S. Stevens, I. Fustos-Toribio, P. I. Moreno, F. Vera, and Á. Amigo (2024). "New perspectives on ice forcing in continental arc magma plumbing systems". *Journal of Volcanology and Geothermal Research* 455, page 108187. DOI: 10.1016/j.jvolgeores.2024.108187.

Stern, R. J., J. Morris, S. H. Bloomer, and J. W. Hawkins (1991). "The source of the subduction component in convergent margin magmas: Trace element and radiogenic isotope evidence from Eocene boninites, Mariana forearc". *Geochimica et Cosmochimica Acta* 55(5), pages 1467–1481. DOI: 10.1016/0016-7037(91)90321-u.

Stracke, A., M. Bizimis, and V. J. M. Salters (2003). "Recycling oceanic crust: Quantitative constraints". *Geochemistry, Geophysics, Geosystems* 4(3). DOI: 10.1029/2001gc000223.

Straub, S. M., A. B. LaGatta, A. L. Martin-Del Pozzo, and C. H. Langmuir (2008). "Evidence from high-Ni olivines for a hybridized peridotite/pyroxenite source for orogenic andesites from the central Mexican Volcanic Belt". *Geochemistry, Geophysics, Geosystems* 9(3). DOI: 10.1029/2007gc001583.

Sun, S.-s. and W. F. McDonough (1989). "Chemical and isotopic systematics of oceanic basalts: implications for mantle composition and processes". *Geological Society, London, Special Publications* 42(1), pages 313–345. DOI: 10.1144/gsl.sp.1989.042.01.19.

Turner, S., B. Bourdon, and J. Gill (2003). "Insights into Magma Genesis at Convergent Margins from U-series Isotopes". *Reviews in Mineralogy and Geochemistry* 52(1), pages 255–315. DOI: 10.2113/0520255.

Turner, S., C. Beier, Y. Niu, and C. Cook (2011). "U-Th-Ra disequilibria and the extent of off-axis volcanism across the East Pacific Rise at 9°30N, 10°30N, and 11°20N: East Pacific Rise off-axis magmatism". *Geochemistry, Geophysics, Geosystems* 12(7). DOI: 10.1029/2010gc003403.

Turner, S. J., C. H. Langmuir, M. A. Dungan, and S. Escrig (2017). "The importance of mantle wedge heterogeneity to subduction zone magmatism and the origin of EM1". *Earth and Planetary Science Letters* 472, pages 216–228. DOI: 10.1016/j.epsl.2017.04.051.

Turner, S. J., C. H. Langmuir, R. F. Katz, M. A. Dungan, and S. Escrig (2016). "Parental arc magma compositions dominantly controlled by mantle-wedge thermal structure". *Nature Geoscience* 9(10), pages 772–776. DOI: 10.1038/ngeo2788.

Watanabe, T., T. Masuyama, K. Nagaoka, and T. Tahara (2002). "Analog experiments on magma-filled cracks: Competition between external stresses and internal pressure". *Earth, Planets and Space* 54(12), e1247–e1261. DOI: 10.1186/bf03352453.

Watt, S. F. L., D. M. Pyle, T. A. Mather, and J. A. Naranjo (2013). "Arc magma compositions controlled by linked thermal and chemical gradients above the subducting slab". *Geophysical Research Letters* 40(11), pages 2550–2556. DOI: 10.1002/grl.50513.

Weis, D., B. Kieffer, C. Maerschalk, J. Barling, J. de Jong, G. A. Williams, D. Hanano, W. Pretorius, N. Mattielli, J. S. Scoates, A. Goolaerts, R. M. Friedman, and J. B. Mahoney (2006). "High-precision isotopic characterization of USGS reference materials by TIMS and MC-ICP-MS". *Geochemistry, Geophysics, Geosystems* 7(8). DOI: 10.1029/2006gc001283.

Williams, R. and J. Gill (1989). "Effects of partial melting on the uranium decay series". *Geochimica et Cosmochimica Acta* 53(7), pages 1607–1619. DOI: 10.1016/0016-7037(89)90242-1.

Winslow, H., P. Ruprecht, M. Stelten, and A. Amigo (2020). "Evidence for primitive magma storage and eruption following prolonged equilibration in thickened crust". *Bulletin of Volcanology* 82(11). DOI: 10.1007/s00445-020-01406-3.

Workman, R. K. and S. R. Hart (2005). "Major and trace element composition of the depleted MORB mantle (DMM)". *Earth and Planetary Science Letters* 231(1–2), pages 53–72. DOI: 10.1016/j.epsl.2004.12.005.